CHEMISTRY OF MATERIALS

pubs.acs.org/cm

Article

Topochemical Reduction of $La_2NiO_3F_2$: The First Ni-Based Ruddlesden–Popper n = 1 T′-Type Structure and the Impact of Reduction on Magnetic Ordering

Kerstin Wissel, Ali Muhammad Malik, Sami Vasala, Sergi Plana-Ruiz, Ute Kolb, Peter R. Slater, Ivan da Silva, Lambert Alff, Jochen Rohrer, and Oliver Clemens*

Cite This: *Chem. Mater.* 2020, 32, 3160–3179

Read Online

ACCESS | Metrics & More | Article Recommendations | Supporting Information

ABSTRACT: Within this study, we show that a broad range of reduced phases $La_2NiO_3F_{2-\Delta}$ can be derived from Ruddlesden–Popper-type $La_2NiO_3F_2$ using a reductive topochemical defluorination method based on reactions between the oxyfluoride and sodium hydride. The selective extraction of fluoride results in strong structural changes, and the nuclear and magnetic structures of the obtained phases have been determined. Due to the high anion content in $La_2NiO_3F_2$, the formation of Ni^+-containing compounds has been observed under reduction. For the first time, this has led to the formation of the highest reduced end member with a T′-type structure with an approximate composition of La_2NiO_3F in the n = 1 Ruddlesden–Popper-type series containing only Ni^+ as the B-cation. This compound can be described as stacking of alternating (La/O_2/La) fluorite-type layers with $La_{n-1}(NiO_2)_n$ infinite layer structural blocks. The underlying reaction mechanism has been investigated by means of X-ray and neutron diffraction, elemental analysis, and magnetic measurements. Furthermore, to gain a deeper understanding of structural distortions, density functional theory-based calculations were performed, providing information about structural rearrangements upon defluorination and magnetic interactions. It is highlighted that the presence of even small amounts of d^9-configured Ni^+ cations leads to strong structural changes in $La_2NiO_3F_{1.93}$, introducing long-range antiferromagnetic ordering between the adjacent perovskite building blocks by increasing the Ni–X–X–Ni super-superexchange interactions as compared to stoichiometric $La_2NiO_3F_2$.

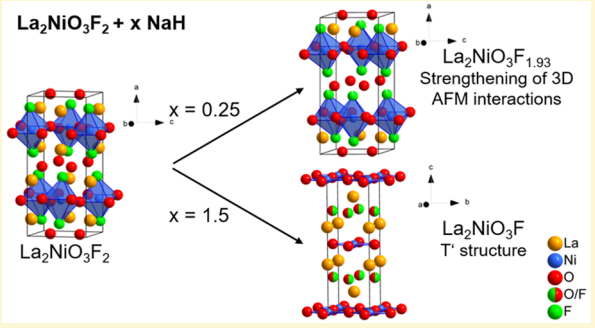

1. INTRODUCTION

Topochemical modifications of transition-metal oxides, especially of perovskites or related Ruddlesden–Popper (RP)-type compounds, allow the synthesis of metastable phases that are inaccessible by conventional high-temperature reactions.[1] This gives the ability to control the oxidation state of the transition metal, which is critical for the development of new materials with defined intrinsic properties. For multinary oxides containing more than one cation species, the control of the transition-metal oxidation state can be achieved via aliovalent substitution of another cation or via manipulation of the anion sublattice. These latter manipulations can cover a wide range from anion exchange to intercalation and extraction. In this respect, low-temperature fluorination methods using gaseous or solid-state reagents (e.g., F_2 gas, NH_4F, metal fluorides (CuF_2, AgF_2, AgF, etc.), XeF_2, fluorinated polymers (poly(tetrafluoroethylene) (PTFE), poly(vinylidene fluoride) (PVDF))) and electrochemical reactions can be used for the stabilization of oxide and fluoride anions within one structure.[2−5] Depending on the reaction method, the fluorination can be oxidizing (fluoride is intercalated into vacant or interstitial sites), nonoxidative (substitution of one oxide by one fluoride and additional intercalation of one fluoride, e.g., in $Sr_2TiO_3F_2$[6,7]), or even reducing (substitution of one oxide by one fluoride, e.g., in $SrFeO_2F$[8]). Other powerful approaches for the manipulation of the anion sublattice are topochemical reduction methods using metal hydrides, leading to anion deintercalation, which can also be accompanied by hydride intercalation.[9]

As indicated above, compounds with the perovskite structure ABO_3 and the RP (also called K_2NiF_4 or T for n = 1) structure $A_{n+1}B_nO_{3n+1}$ (Figure 1, left) have been investigated widely. The perovskite-related Ruddlesden–Popper structure can be described as n ABO_3 perovskite building blocks separated by AO rock-salt layers. Additional anions can be intercalated into vacant interstitial sites, which are located

Received: January 16, 2020
Revised: February 6, 2020
Published: February 6, 2020

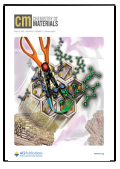

https://dx.doi.org/10.1021/acs.chemmater.0c00193
Chem. Mater. 2020, 32, 3160–3179

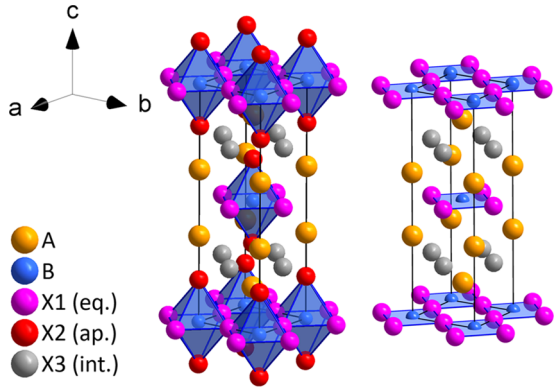

Figure 1. (Left) Schematic drawing of the $n = 1$ Ruddlesden–Popper-type (K_2NiF_4-type or T-type) structure with composition $A_2BX1_2^{eq}X2_2^{ap}X3_2^{int}$; (right) schematic drawing of the $n = 1$ T′-type structure with composition $A_2BX1_2^{eq}\square_2^{ap}X3_2^{int}$. Equatorial (eq.), apical (ap.), and interstitial (int.) anion sites are shown with different colors. In the stoichiometric T-type compounds, the interstitial anion site is not occupied.

where the rock salt and the perovskite building blocks interpenetrate each other.

Prominent examples for topochemical reactions can be found in cuprates derived from the RP-type La_2CuO_4 ($n = 1$) and its higher-order members ($n = 2$, 3), leading to the observation of high-temperature superconductivity.[10−17] On these compounds, numerous studies on the influence of cation substitution, oxygen overstoichiometry, and fluoride incorporation have been performed. After the discovery of superconductivity in cuprates, nickelates have also been considered promising candidates for superconductivity due to the isoelectronic configuration of Cu^{3+}/Cu^{2+} and Ni^{2+}/Ni^{+} (d^9/d^8).[18−20] Theoretical studies predict that superconductivity can only be evoked in nickelates with Ni^{2+}/Ni^{+} in square-planar coordination forming infinite NiO_2 layers.[18] Interestingly, all known nickelates having infinite NiO_2 square-planar layers are members of the T′-type $Ln_{n+1}Ni_nO_{2n+2}$ (Ln = La, Nd, Pr; $n = 2$, 3, ∞) homologous series.[21−27] For example, the deoxygenation of $La_3Ni_2O_7$ and $La_4Ni_3O_{10}$ leads to the formation of $La_3Ni_2O_6$ and $La_4Ni_3O_8$, respectively. These T′ structures can be described as stacking of alternating (La/O_2/La) fluorite-type layers and $La_{n-1}(NiO_2)_n$ infinite layer structural blocks. So far, only the so-called double ($n = 2$) and triple ($n = 3$) layer T′-type nickelates have been reported.[24,25]

In analogy to $La_3Ni_2O_6$ and $La_4Ni_3O_8$ (Table 1, which illustrates the Ni oxidation states and anion site occupations in lanthanum nickelates and lanthanum nickel oxyfluorides and their reduced compounds), it could be assumed that a reduction of La_2NiO_4 ($n = 1$) to La_2NiO_{4-d} would lead to the formation of the single ($n = 1$) layer T′-type structure (Figure 1, right). For this compound, the formation of significant amounts of monovalent Ni species would result in a considerable number of vacancies d. Despite the great research interest into low-valent nickelates in the field of high-temperature superconductors in the recent years, this T′-type structure has not been reported for the $n = 1$ member of the RP series $La_{n+1}Ni_nO_{3n+1}$ so far. This might be related to the fact that the anion deficiency d on the interstitial site would result in low-coordination numbers of the A-site cation making it structurally implausible. For strongly reduced phases with the $RP_{n=1}$ structure type, e.g., $LaSrNiO_{3.1}$,[2828] anion vacancies on the equatorial site have been observed, which results in chains of square-planar-coordinated cations instead of layers.

To avoid such an anion deficiency while still being able to reduce the compound and stabilize the T′-type structure, a topochemical modification leading to the introduction of additional anions into the parent compound might be a suitable approach. In this context, the polymer-based low-temperature fluorination of La_2NiO_{4+d} to $La_2NiO_3F_2$ using poly(vinylidene fluoride) (PVDF) as the fluorination reagent was already shown to facilitate the incorporation of more anions via a coupled substitution/insertion process, in which one O^{2-} is replaced by two F^- under the maintenance of the Ni^{2+} oxidation state.[29]

A subsequent reductive metal-hydride-based defluorination might further allow for the synthesis of a single ($n = 1$) layer T′-type nickel oxyfluoride with a composition of La_2NiO_3F. This defluorination strategy was suggested by our group recently.[30,31] It was shown that sodium hydride (NaH) is a good candidate for the selective extraction of fluoride species from $Sr_2TiO_3F_2$ and $Sr_3Ti_2O_5F_4$ due to the high stability of the reaction product NaF.[30]

The introduction of additional anions while maintaining a Ni^{2+} oxidation state (five anions per formula unit in $La_2NiO_3F_2$ instead of four anions per formula unit in La_2NiO_4) might be crucial to obtain the $n = 1$ T′-type structure. For $La_2NiO_3F_2$, one F^- anion could be removed before an anion deficiency on the interstitial site (less than four anions per formula unit) would be generated (Table 1). Furthermore, by reducing $La_2NiO_3F_2$ to La_2NiO_3F, a Ni valence as low as +1 might be achieved. In contrast, only higher Ni valences of +1.5 and +1.33 could be achieved for previously studied $La_3Ni_2O_6$ and $La_4Ni_3O_8$.[24−27]

The layered structure of RP-type compounds $A_{n+1}B_nO_{3n+1}$ leads to highly anisotropic magnetic exchange interactions with overall low effective magnetic moments.[32−34] A decreased dimensionality (low n) corresponds to a decreasing strength of magnetic interactions in the c-direction via the rock-salt building blocks. In particular for $n = 1$, quasi-two-dimensional B–O–B networks are formed, which are separated by the nonmagnetic rock-salt layers. The in-plane (within the ab-

Table 1. Comparison between $n = 1$, 2, 3, ∞ Ruddlesden–Popper-Type and Reduced T′-Type Lanthanum Nickelates and $n = 1$ Ruddlesden–Popper-Type and Reduced T′-Type Lanthanum Nickel Oxyfluorides[a]

	Ruddlesden–Popper structure of oxide	T′ structure of reduced oxide	Ruddlesden–Popper structure of oxyfluoride	T′ structure of reduced oxyfluoride
$n = 1$	$La_2Ni^{2+}O_2^{eq}O_2^{ap}O^{int}$	$La_2Ni^{(2-2d)+}O_2^{eq}O_2^{ap}O_{2-d}^{int}$	$La_2Ni^{2+}O_2^{eq}O_2^{ap}F_2^{ap}F^{int}O^{int}$	$La_2Ni^{+}O_2^{eq}O_2^{ap}O^{int}F^{int}$
$n = 2$	$La_3Ni_2^{2.5+}O_4^{eq}O_3^{ap}O_2^{int}$	$La_3Ni_2^{1.5+}O_4^{eq}O_3^{ap}O_2^{int}$		
$n = 3$	$La_4Ni_3^{2.67+}O_6^{eq}O_4^{ap}O_2^{int}$	$La_4Ni_3^{1.33+}O_6^{eq}O_4^{ap}O_2^{int}$		
$n = \infty$	$LaNi^{3+}O_3$	$LaNi^{+}O_2$		

[a]Also given are the Ni oxidation states and occupations of anion sites of the different compounds.

https://dx.doi.org/10.1021/acs.chemmater.0c00193
Chem. Mater. 2020, 32, 3160−3179

plane) exchange interactions are mediated via B−O−B bonds, while the interbilayer (out of plane along the *c* axis) exchange takes place via B−X−X−B (X being oxide or fluoride ions). The interactions can be ferromagnetic or antiferromagnetic (AFM), depending on whether the dominating interaction is double exchange or superexchange, respectively. The introduction of additional anions into the interstitial site, further, increases the distances between adjacent layers, reducing the exchange interactions significantly since they take place over longer distances and/or possibly over a larger number of anions (e.g., B−X−X−X−B). With respect to the type of anion, interactions via oxide ions are known to be stronger as compared to fluoride ions.[35]

In this article, we report on the preparation of low-valent nickel compounds via hydride-based reductions of $La_2NiO_3F_2$ using sodium hydride. The reaction mechanism was studied via a combination of methods (X-ray (XRD) and neutron powder diffraction (NPD), elemental analysis, and magnetic measurements). Furthermore, the nuclear and magnetic structures of the obtained phases were derived. Quantum chemical calculations help in providing insights into the reaction mechanism, structural rearrangement processes, and their impact on the magnetic interactions. This way, a broad range of new fluoride extracted compounds was found, in which the reduction induces unusual strengthening of antiferromagnetic ordering between the perovskite-type layers of $RP_{n=1}$ compounds.

2. EXPERIMENTAL SECTION

2.1. Synthesis of La_2NiO_{4+d} and $La_2NiO_3F_2$. The precursor oxide La_2NiO_{4+d} was synthesized by a solid-state reaction of previously dried (700 °C, 4 h, Ar) high-purity La_2O_3 (Alfa Aesar, 99.9%) and NiO (Alfa Aesar, 99%). The starting materials were mixed in stoichiometric amounts using a planetary ball-mill (ZrO_2 grinding jar and balls, 250 rpm, 30 min) and heated to 1200 °C for 12 h in air with an intermediate regrinding step. The oxyfluoride $La_2NiO_3F_2$ was prepared by chemical fluorination of La_2NiO_{4+d} using the fluorination agent poly(vinylidene fluoride) $(CH_2CF_2)_n$ (PVDF, Sigma-Aldrich). The as-prepared precursor oxide was mixed with PVDF with 2.5% excess and heated to 370 °C for 24 h in air.

2.2. Topochemical Reductions of $La_2NiO_3F_2$. The reductions of $La_2NiO_3F_2$ were performed using NaH (dry, 95%, Sigma-Aldrich) as the reducing agent. The oxyfluoride was intimately ground with NaH using a mortar and pestle in an Ar-filled glovebox according to eq 1

$$La_2NiO_3F_2 + x\mathrm{NaH} \quad (1)$$

Since side reactions are known to occur for Ni-containing compounds (e.g., the formation of metallic Ni),[22] an increased range of NaH equivalents was studied, $0.25 \le x \le 2$ ($\Delta x = 0.25$). Additionally, one reduction was performed using a large excess of NaH ($x = 2.5$). The different mixtures were subsequently placed into corundum crucibles, sealed in stainless steel vacuum-tight reactors equipped with oil bubblers to avoid the buildup of overpressure, and heated to 300 °C for 48 h. After the reaction, the reactor was opened inside an Ar-filled glovebox and the sample was removed.

2.3. Re-Oxidation and Re-Fluorination of Reduction Reaction Products. Reacted phase mixtures $La_2NiO_3F_2 + x\mathrm{NaH}$ with $x = 0.5$, 1, and 1.5 were intentionally re-oxidized by heating them to 350 °C for 4 h in air.

The re-fluorination experiments on $La_2NiO_3F_2 + x\mathrm{NaH}$ with $x = 1$ and 1.5 were performed using flowing F_2 (10% in N_2) at temperatures between 50 and 300 °C for durations of 15 min.

2.4. X-ray and Neutron Diffraction Experiments. X-ray diffraction (XRD) patterns were recorded on a Bruker D8 Advance diffractometer in Bragg−Brentano geometry with Cu Kα radiation and a VANTEC detector. For phase quantification of the reacted samples of $La_2NiO_3F_2 + x\mathrm{NaH}$ ($0.25 \le x \le 2.5$), the samples were measured in a 2θ range between 20 and 70° using a fixed divergence slit for ∼4 h. The high-quality data for the Rietveld refinements of $La_2NiO_3F_2 + x\mathrm{NaH}$ with $x = 0.25$, 0.5, 1, and 1.5 were recorded using a variable divergence slit of 6 mm with measurement times of ∼17.5 h in the angular range of 20−130°. All samples were measured inside low-background airtight specimen holders (Bruker A100B36/B37), which were sealed inside an Ar-filled glovebox.

Time-of-flight (TOF) neutron powder diffraction (NPD) data[36] were recorded on the GEM diffractometer at the ISIS pulsed spallation source (Rutherford Appleton Laboratory, U.K.).[37,38] Approximately 1.5 g of $La_2NiO_3F_2$ or the reacted samples of $La_2NiO_3F_2 + x\mathrm{NaH}$ with $x = 0.25$, 0.5, 1, and 1.5 were loaded into 6 mm diameter thin-walled, airtight-sealed cylindrical vanadium sample cans. For the measurements of $La_2NiO_3F_2$, data were collected at ambient temperature, 100, 55, and 10 K for 170 μAh proton beam current to the ISIS target (corresponding to ∼1 h of beam time). The reacted samples of $La_2NiO_3F_2 + x\mathrm{NaH}$ with $x = 0.25$, 0.5, 1, and 1.5 were measured at ambient temperature, 100 K, and 10 K for 510 to 850 μAh proton beam current (corresponding to ∼3−5 h of beam time). The time-of-flight data were normalized to the incident spectrum and corrected for detector efficiency by reference to a V/Nb standard using the Mantid suite of diffraction utilities.[3939]

Analysis of diffraction data was performed using the Rietveld method with the program TOPAS V. 5.0[40,41] using the whole XRD data 2θ range as well as the data recorded on all diffraction banks of the TOF neutron powder diffractometer. The instrumental intensity distributions of the XRD and NPD instruments were determined empirically from a sort of fundamental parameters set[42] using a reference scan of LaB_6 (NIST 660a) and silicon (NIST SRM640c), respectively. The microstructural parameters (crystallite size and strain broadening) were refined to adjust the peak shapes. Thermal displacement parameters were constrained to be the same for all atoms of all phases to minimize quantification errors and correlation with occupancy parameters. Note that quantification errors are on the order of 1−2 wt %, at least for the phase quantities given in the article; numerical errors obtained from the refinement are known for not representing a reasonable interval of trust, and so error bars of the numerical errors are omitted for the graphical representations of phase quantities.

For the determination of the magnetic structure, the magnitude, and the orientation of magnetic moments, refinements were performed on GEM bank 3 data only.

For the determination of amorphous phase contents, the reduced samples were mixed in a defined weight ratio with the standard LaB_6 (Sigma-Aldrich, 99%) and XRD patterns were recorded. The calculation of the respective amorphous fraction was performed using the internal standard method, as implemented in TOPAS v.5.0.

2.5. Elemental Analysis. Elemental analysis was performed on a VarioEL III CHN (Elementar). Samples were heated in Sn boats under oxygen, and the evolving gases were gas chromatographically separated and analyzed quantitatively with a thermal conductivity detector. The hydride content was determined as the mean of four measurements.

2.6. Transmission Electron Microscopy Characterization. Samples of $La_2NiO_3F_2$ and the reduction reaction products $La_2NiO_3F_2 + x\mathrm{NaH}$ with $x = 0.25$ and 1.5 were prepared by placing a drop of a dispersion of the respective powder in *n*-hexane on a carbon-coated copper grid. A FEI Tecnai F30 S-TWIN transmission electron microscope (TEM) equipped with a field emission gun and operated at 300 kV was used. For fast and automated diffraction tomography (Fast-ADT) experiments,[43,44] a 10 μm condenser aperture, spot size 6, and gun lens 8 were set to produce a quasiparallel beam of 200 nm in size. For the identification of Ni-containing particles, energy-dispersive X-ray (EDX) spectroscopy measurements were conducted with a 50 μm condenser aperture, spot size 6, and gun lens 1 to increase the electron dose and have a reliable amount of counts on the EDX detector (EDAX EDAM III). Scanning transmission electron microscopy (STEM) images were collected

https://dx.doi.org/10.1021/acs.chemmater.0c00193
Chem. Mater. 2020, 32, 3160−3179

using a Fischione high-angle annular dark-field (HAADF) detector. Electron diffraction patterns were acquired with an UltraScan4000 charge-coupled device (CCD) camera provided by Gatan (16 bit, 4096 × 4096 pixels). Hardware binning 2 and an exposure time of 1 s were used to acquire nonsaturated diffraction reflections. Fast-ADT data sets were acquired with an automated acquisition module developed for FEI and JEOL microscopes, which allows the acquisition of electron diffraction tomographies in around 10 min for conventional CCD cameras and fixed tilt step of 1°. Precession electron diffraction (PED)[45] was coupled to the Fast-ADT data collection to minimize the dynamical effects and improve the reflection intensity integration quality.[46] PED was generated by means of the DigiStar system developed by NanoMegas SPRL, and it was kept to 1°.

Three-dimensional processing of the Fast-ADT data was done by the eADT software package.[47] Sir2014[48] was used for ab initio structure solution, and Jana2006[49] was later used for crystal structure refinement. Intensity extraction for dynamical refinement was done by PETS2.[50] EDX peak identification and quantification were carried out by the ES Vision software.

2.7. Magnetic Measurements. Magnetic characterization was performed with a Quantum Design MPMS-3 Squid VSM. Powder samples were placed and sealed in gelatin capsules and mounted in a straw. Zero-field-cooled (ZFC) and field-cooled (FC) curves were measured in the temperature region from 5 to 300 K in the applied field $\mu_0 H$ = 1 T. Field-dependent measurements were performed at 10, 100, and 300 K. The magnetic field was scanned from 5 to −5 T.

2.8. Density Functional Theory (DFT) + *U* Calculations. The DFT calculations were performed using the Vienna ab initio simulation package (VASP)[51,52] by employing the projector-augmented wave (PAW)[53,54] method for pseudopotential and plane wave expansion of wave functions. The Perdew−Burke−Ernzerhof (PBE)[55] form of the generalized gradient approximation (GGA) for the exchange-correlation functional along with the +*U* correction as proposed by Dudarev et al.[56] was used to account for strong localization of the d-orbitals of transition-metal (Ni) ions, which is not well described in standard GGA. The difference of *U* and *J* parameters known as U_{eff} bears importance for the currently utilized +*U* model. The $U_{eff} = U - J$ for all compounds was selected to be 6 eV, lying within a suitable *U* range for nickelate compounds.[18,57] The parameter *J* was fixed at 0 eV for all calculations. The energy cutoff for the plane wave basis set was chosen to be 600 eV. The reciprocal space was sampled by a Monkhorst−Pack-type[58] Γ-centered *k*-mesh of 2 × 4 × 5. During structural optimization, the forces were converged within 0.01 eV/Å for each atom. All degrees of freedom without symmetry constraint were allowed during structural relaxations unless mentioned otherwise. The energy criterion for convergence of the electronic self-consistency was set to 1×10^{-6} eV. The utilized pseudopotentials treated 7, 11, 10, and 6 electrons as part of the valence band of F, La, Ni, and O atoms, respectively.

3. RESULTS AND DISCUSSION

3.1. Topochemical Reduction of $La_2NiO_3F_2$. *3.1.1. Analysis of the Reduction Mechanism.* The topochemical fluorination of La_2NiO_{4+d} to $La_2NiO_3F_2$ (a = 12.8473(2) Å, b = 5.79922(8) Å, c = 5.49222(10) Å, $V_{f.u.}$ = 204.60(1) Å^3) leads to a symmetry lowering from *I*4/*mmm* to *Cccm*. The structural distortion is caused by a channel-like ordering of oxide ions on the interlayer sites, leading to an expansion of the lattice perpendicular to the stacking direction, accompanied by a strong tilting of the NiO_4F_2 octahedra.[29] This unusual anion ordering might have interesting effects on the structure of the defluorinated phases. Depending on the used synthesis batch of the parent oxide La_2NiO_{4+d}, either phase pure samples are formed or additionally a small amount of $La_{0.5}Zr_{0.5}O_{1.75}$ (∼1 wt %) is found. Presumably, the impurity phase is formed due to the use of a ZrO_2 grinding jar and balls during the ball-milling process. The phase fraction of this impurity phase, if found in La_2NiO_{4+d} and $La_2NiO_3F_2$, remains constant in the defluorinated products.

For the topochemical reduction of $La_2NiO_3F_2$, various mixtures of $La_2NiO_3F_2$ + xNaH were reacted and investigated by means of X-ray diffraction (Figure 2). Neglecting

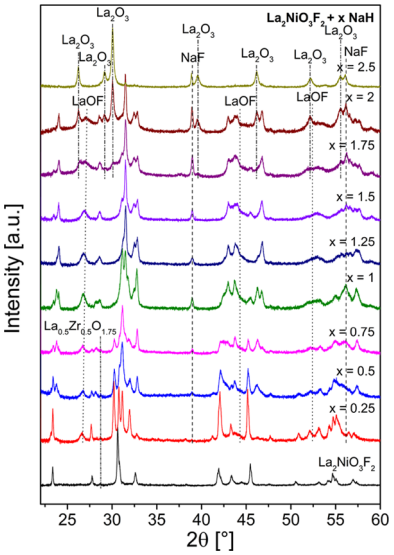

Figure 2. X-ray diffraction patterns of $La_2NiO_3F_2$ and the products obtained after the reaction of $La_2NiO_3F_2$ with xNaH ($0.25 \leq x \leq 2.5$). For the Rietveld refinements of the patterns shown together with an assignment of reflections to $La_2NiO_3F_2$ and the reduced phases monoclinic $La_2NiO_3F_{2-a}$, orthorhombic #1 $La_2NiO_3F_{2-b}$, orthorhombic #2 $La_2NiO_3F_{2-c}$, and tetragonal $La_2NiO_3F_{2-d}$, the reader is referred to Figure S1 in the Supporting Information.

decomposition during the reaction, the reaction equation of the desired reduction takes place according to eq 2 (for $x \leq 1$).

$$La_2NiO_3F_2 + x\mathrm{NaH} \rightarrow La_2NiO_3F_{2-x} + x\mathrm{NaF} + \frac{x}{2}H_2 \quad (2)$$

Depending on the amount x of added NaH, phase mixtures of phases with different fluoride contents and strongly different structures are formed, visually evident from the strong shifts and splitting of reflections in comparison to $La_2NiO_3F_2$. By studying the broad range of compositions, the following four phases (given in the order of appearance for increasing x) were identified: monoclinic $La_2NiO_3F_{2-a}$, orthorhombic #1 $La_2NiO_3F_{2-b}$, orthorhombic #2 $La_2NiO_3F_{2-c}$, and tetragonal $La_2NiO_3F_{2-d}$. The metastability of $La_2NiO_3F_2$ and the necessity to reduce reaction temperatures can be considered as possible limitations to obtain phase pure samples. In particular, the reaction chemistry must be carefully balanced between the energetic stability of the reaction products, kinetic limitations to reach the energetically most stable reaction products, and the metastability of the educt. Rietveld analysis of XRD data was performed for all compositions studied; the crystal structures of the above given phases were analyzed by coupled analysis of X-ray and neutron powder diffraction data (see Section 3.1.2.1; the refined patterns of the reacted mixtures $La_2NiO_3F_2$ + 0.25NaH, $La_2NiO_3F_2$ + 0.5NaH, and $La_2NiO_3F_2$ + 1.5NaH, from which the used structural models of the four phases were deducted, are shown in Figures 4, 7, and 8, respectively). Each phase has a distinctive set of lattice parameters with a nearly constant volume per formula unit

https://dx.doi.org/10.1021/acs.chemmater.0c00193
Chem. Mater. 2020, 32, 3160−3179

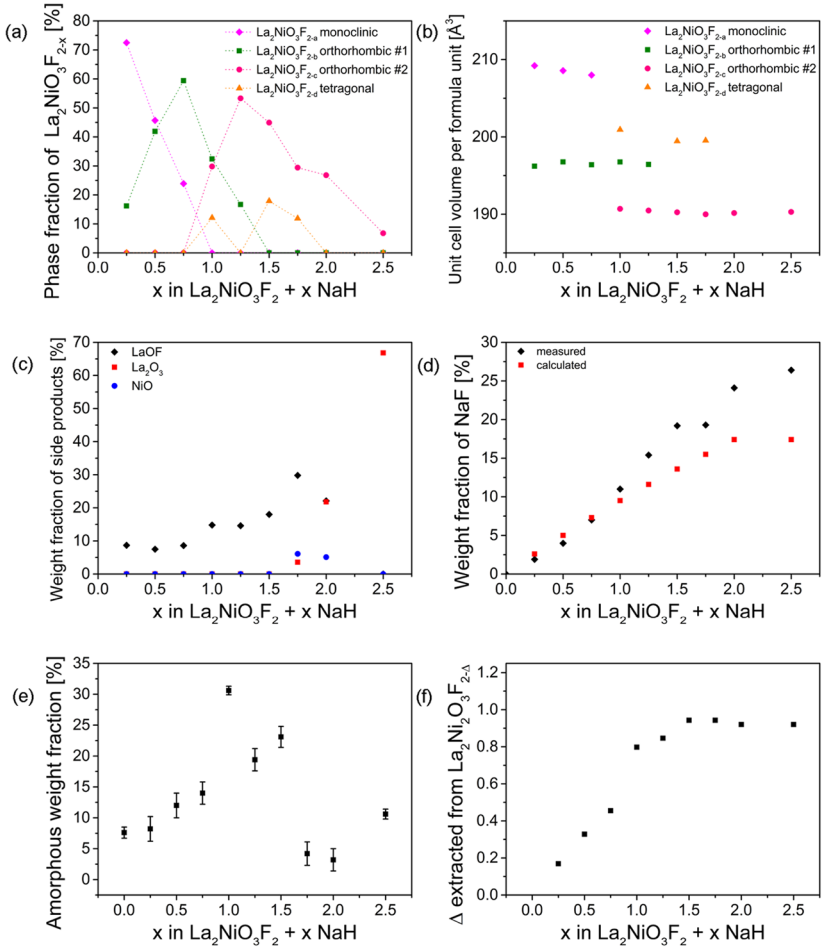

Figure 3. (a) Weight fractions of $La_2NiO_3F_2$ and reduced phases $La_2NiO_3F_{2-a}$, $La_2NiO_3F_{2-b}$, $La_2NiO_3F_{2-c}$, and $La_2NiO_3F_{2-d}$ in reduction reaction products $La_2NiO_3F_2$ + xNaH ($0.25 \leq x \leq 2.5$) not including amorphous weight fractions as a function of x; (b) unit-cell volumes per formula unit of $La_2NiO_3F_2$ and reduced phases $La_2NiO_3F_{2-a}$, $La_2NiO_3F_{2-b}$, $La_2NiO_3F_{2-c}$, and $La_2NiO_3F_{2-d}$ in reduction reaction products $La_2NiO_3F_2$ + xNaH ($0.25 \leq x \leq 2.5$) as a function of x; (c) weight fractions of decomposition products in reduction reaction products $La_2NiO_3F_2$ + xNaH ($0.25 \leq x \leq 2.5$) not including amorphous weight fractions as a function of x; (d) weight fractions of NaF in reduction reaction products $La_2NiO_3F_2$ + xNaH ($0.25 \leq x \leq 2.5$) not including amorphous weight fractions as a function of x, together with theoretically expected values calculated assuming full conversion to NaF from the amount of NaH added; (e) amorphous weight fractions in reduction reaction products $La_2NiO_3F_2$ + xNaH ($0.25 \leq x \leq 2.5$) as a function of x; (f) values of extracted fluoride Δ in $La_2NiO_3F_{2-\Delta}$ (calculated using the relative weight fractions and occupation factors as obtained from coupled Rietveld analysis of reduced phases) as a function of x.

(Figure 3a) within their range of existence. A detailed list of refined lattice parameters, unit-cell volumes, and phase fractions is given in Table S1. Compared to that of $La_2NiO_3F_2$, the volumes of the orthorhombic phases $La_2NiO_3F_{2-b}$ and $La_2NiO_3F_{2-c}$ decrease significantly with increasing defluorination. The monoclinic phase $La_2NiO_3F_{2-a}$ has an increased volume and the tetragonal phase $La_2NiO_3F_{2-d}$ shows a slightly decreased volume, although strong changes of lattice parameters are found.

The evolution of the weight fractions of obtained phases as a function of x is given in Figure 3b. For $x = 0.25$, the majority of the samples consist of the monoclinic phase, with the orthorhombic #1 phase being present in addition. While the phase fraction of the monoclinic phase is continuously decreasing for values $0.25 \leq x \leq 0.75$, the orthorhombic #1 phase becomes the main phase for increasing x. For $x \geq 1$, the phase fraction of the orthorhombic #1 phase is reducing, and additionally, a second orthorhombic #2 phase and a tetragonal phase are formed. The phase fractions of these phases increase subsequently before they decrease drastically. This strong decrease for $x \geq 1.75$ suggests a substantial decomposition of the former RP-type phases (the possibility of decomposition due to water and a resulting HF release can be ruled out since the samples were prepared, stored, and characterized under an Ar atmosphere (< 0.1 ppm H_2O)). This also becomes evident with respect to the formation of decomposition products (LaOF, NiO, La_2O_3) (Figure 3c), as well as on comparing the amount of formed NaF to the hypothetical amount in a product containing only crystalline phases (Figure 3d). A strong increase of LaOF and the considerable divergence between the weight fraction of measured and calculated NaF (assuming a complete reaction of used NaH to NaF since no unreacted NaH or NaOH is present) starts already at $x = 1$. In contrast, the formation of La_2O_3 can only be observed for $1.75 \leq x$. For $x = 2.5$, besides La_2O_3, only ∼7 wt % of the orthorhombic phase #2 is found. The presence of crystalline Ni (or NiO), which should be formed during decomposition, could not be confirmed by means of diffraction (except for $x = 1.75$ and 2, where a very small phase fraction of NiO is observed) possibly since it may form amorphous or nanocrystalline clusters. Indication for the formation of an amorphous Ni-containing phase is given in reaction product

https://dx.doi.org/10.1021/acs.chemmater.0c00193
Chem. Mater. 2020, 32, 3160−3179

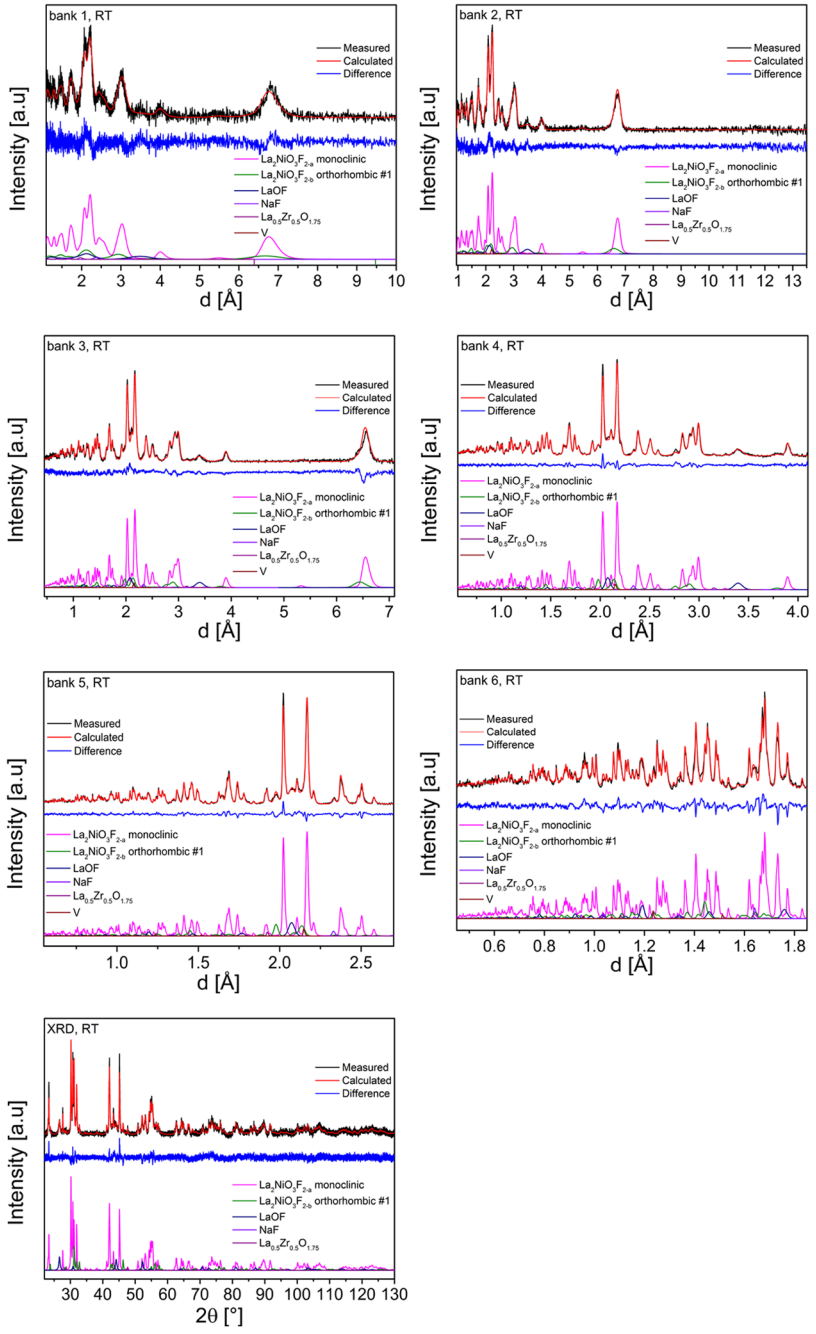

Figure 4. Coupled Rietveld analysis of $La_2NiO_3F_2$ + 0.25NaH of GEM bank 1−6 NPD and XRD data measured at room temperature (RT), from which the structural model of monoclinic $La_2NiO_3F_{2-a}$ (approximate composition: $La_2NiO_3F_{1.93}$) was derived. The structural model for $La_2NiO_3F_{2-b}$ was derived from the coupled Rietveld analysis of $La_2NiO_3F_2$ + 0.5NaH.

with large excess of NaH (x = 2.5), in which, even though no crystalline Ni phase can be found at all, a very broad bump is found between 43 and 46° 2θ (see Figure S2 in the Supporting Information). This angular range coincides with the range in which the scattering of amorphous Ni has been reported.[59] The highest-intense (111) reflection of crystalline Ni would be expected at ∼44° 2θ.[60] However, magnetic measurements give a clear indication for the existence of ferromagnetic Ni (see Section 3.1.3.1), especially with regards to the antiferromagnetic ordering found for the reduced compounds. The partial decomposition on reduction can be confirmed further by determining the amorphous weight fractions (Figure 3e) within the reaction products using the method of an internal standard. For 0.25 ≤ x ≤ 1.5, a continuous increase of the amorphous weight fractions is found (it is emphasized that the outlier of x = 1 could be reproduced within three attempts). Remarkably, for 1.75 ≤ x ≤ 2.5, the amorphous phase fractions decrease again, indicating a re-crystallization on the formation of the final decomposition product La_2O_3.

From the broad range of samples measured, a set of competing reactions as well as decomposition reactions (eqs 3−5) can be formulated, which explain the reaction products and variety of phases found, highlighting the most plausible reaction mechanism

https://dx.doi.org/10.1021/acs.chemmater.0c00193
Chem. Mater. 2020, 32, 3160−3179

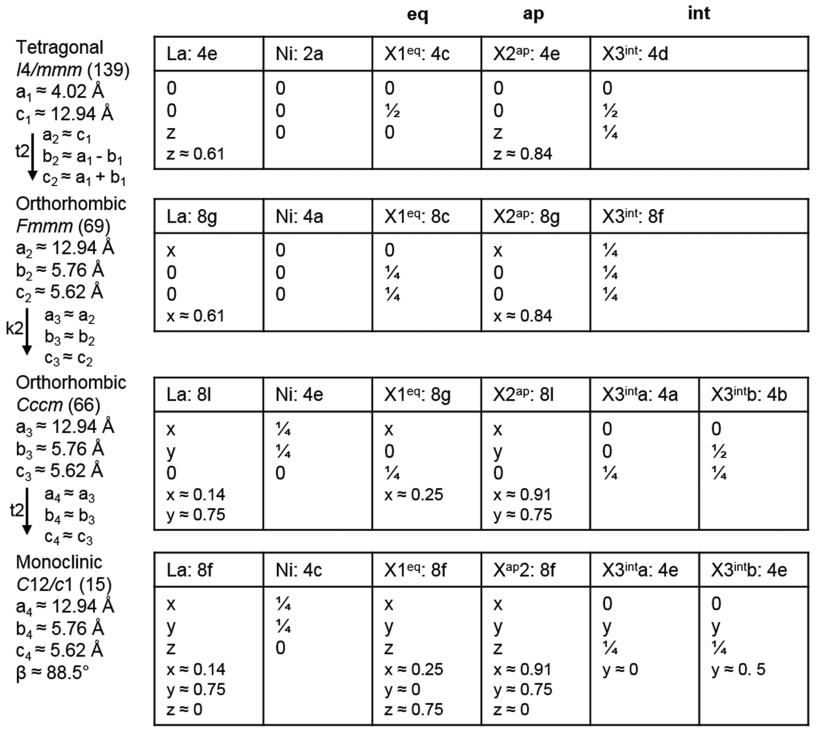

Figure 5. Symmetry tree for the symmetry reduction from the aristotype $RP_{n=1}$ with $I4/mmm$ symmetry to $Cccm$ of $La_2NiO_3F_2$ to $C12/c1$ of $La_2NiO_3F_{2-a}$. Equatorial (eq), apical (ap), and interstitial (int) sites of the anions X (O^{2-} or F^-) are indicated (see also structural data reported in Table 2).

Decomposition reactions:

$$La_2NiO_3F_2 + xNaH \rightarrow 2LaOF + Ni + xNaOH + \frac{1-x}{2}O_2 \quad (3)$$

$$La_2NiO_3F_2 + 2NaH \rightarrow La_2O_3 + Ni + 2NaF + H_2 \quad (4)$$

Partial fluoride−oxide exchange:

$$La_2NiO_3F_{2-x} + yLa_2O_3 \rightarrow La_2NiO_{3+y}F_{2-x-y} + 2yLaOF\ (x + y = \Delta) \quad (5)$$

Since no NaOH was observed, a reaction according to eq 3 seems unlikely. This phase could also not be observed in our previous studies on the reduction of $Sr_2TiO_3F_2$[30] and $Sr_3Ti_2O_5F_4$,[3131] which do not show significant amorphization.

LaOF is found for $x \leq 1.75$, while La_2O_3 (eq 4) is only present for $x \geq 1.75$. This fact might be explained by a partial fluoride−oxide exchange between $La_2NiO_3F_{2-\Delta}$ and La_2O_3, according to eq 5, which could be facilitated for the fluoride-richer RP phases at low values of x. Taking this into account (together with the fact that more than one RP-type phase is present especially for high values of x), it is clear that a detailed determination of the anion composition, i.e., the O/F ratio, of the reduced phases is not possible. However, the neutron diffraction studies allow for the approximate determination of an anion content of each phase. Nevertheless, the consistency of the structural changes together with the quantification of the reaction products renders the above-described defluorination mechanism the most likely scenario.

The occupation factors of the different anion sites of the reduced phases (as obtained from the couple Rietveld analysis, see Section 3.1.2) allow for an estimation of the composition of each individual phase. Weighted by the relative phase fraction of the phases derived from $La_2NiO_3F_2$ (not taking decomposition and side products, fluoride−hydride substitution (see below), or amorphization into account), an approximate overall value of Δ with Δ being the fluoride extracted from $La_2NiO_3F_{2-\Delta}$ can be determined for a specific x (Figure 3f). While for values $0.25 \leq x \leq 0.75$ a steady increase in Δ can be observed, Δ adopts values between ∼0.81 and 0.94 for higher x. This seems to be reasonable since a theoretical extraction of more than one fluoride ion from $La_2NiO_3F_2$ would correspond to the formation of metallic nickel (or an average nickel oxidation state below +1) within the reduced compound, which is chemically implausible. It might be, further, possible to extract more fluoride if a (partial) fluoride−hydride substitution takes place. Elemental analysis indicates, however, that this occurs only to a small extent ($La_2NiO_3F_{2-\Delta}H_{0.12(2)}$ for $x = 0.25$ and 0.5; $La_2NiO_3F_{2-\Delta}H_{0.17(2)}$ for $x = 1$; $La_2NiO_3F_{2-\Delta}H_{0.21(4)}$ for $x = 1.5$). The hydride contents are significantly lower as compared to the reduction of $Sr_2TiO_3F_2 + xNaH$, where the average compositions of $Sr_2TiO_3FH_{0.48(1)}$ and $Sr_2TiO_3H_{1.48(10)}$ were found for $x = 1$ and 2, respectively.[30] From the diffraction analysis, it was not possible to assign the residual hydride ions to one of the phases or to the amorphous phase fraction.

Further support of the proposed reaction mechanism can be obtained by re-oxidation and re-fluorination experiments of the reduced samples. After the exposure of the reduction reaction products $La_2NiO_3F_2 + xNaH$ with $x = 0.5$, 1, and 1.5 to air at elevated temperatures, phase mixtures with several re-oxidized phases are found (Figure S3). Phases with similar lattice parameters were found when the parent oxide La_2NiO_{4+d} was fluorinated with varying nonstoichiometric amounts of PVDF to $La_2NiO_{3+y/2}F_{2-y}$;[61] this, together with the fact that

https://dx.doi.org/10.1021/acs.chemmater.0c00193
Chem. Mater. 2020, 32, 3160−3179

Table 2. Structural Parameters of Monoclinic $La_2NiO_3F_{2-a}$ (Approximate Composition: $La_2NiO_3F_{1.93}$) from Coupled Analysis of X-ray and Neutron Diffraction Data of $La_2NiO_3F_2$ + 0.25NaH

	Wyckoff site	x	y	z	occupancy	thermal displacement (Å^2)
La1	8f	0.1123(7)	0.7483(3)	−0.0236(2)	1	0.88(1)
Ni1	4c	1/4	1/4	0	1	0.88(1)
O1 at X1^{eq}	8f	0.2704(1)	−0.0317(3)	0.7771(3)	1	0.88(1)
F2 at X2^{ap}	8f	0.9118(1)	0.8445(2)	−0.0330(3)	0.964(3)	0.88(1)
X3a^{int}	4e	0	0	1/4	0	0.88(1)
O2 at X3b^{int}	4e	0	0.5177(5)	1/4	1	0.88(1)
a (Å)	12.9413(4)		b (Å)	5.7608(2)		
c (Å)	5.6186(2)		β (deg)	88.509(2)		
R_{wp}(XRD + NPD) (%)	3.40	GOF(XRD + NPD)	1.66	R_{bragg} (%)	1.73 (XRD) 3.70 (NPD, bank 3)	
space group	$C12/c1$					

$La_2NiO_3F_2$ cannot be reformed on re-oxidation, supports the extraction of fluoride ions on the topochemical reduction, in agreement with the formation of NaF. Furthermore, the re-fluorination of the reduction reaction products $La_2NiO_3F_2$ + xNaH with x = 1 and 1.5 was attempted using F_2 gas at various temperatures (Figure S4). A re-fluorination could only be obtained within a narrow temperature range; for this reaction, progressive decomposition occurs in parallel. Instead of the synthesis of the desired $La_2NiO_3F_2$, $La_2NiO_3F_{2+x}$ with a considerably increased c lattice parameter was found due to difficulties in controlling the extent of fluorination when using F_2 gas. Nevertheless, the successful fluorination demonstrates the reversibility of the reduction process and confirms the reaction mechanism.

3.1.2. Structural Characterization of Reduction Products. 3.1.2.1. Coupled Rietveld Analyses of Reduction Reaction Products. For the determination of the nuclear structures of the four reduced phases, coupled Rietveld analyses of room-temperature XRD and NPD data were performed on reacted samples of $La_2NiO_3F_2$ + xNaH with x = 0.25, 0.5, 1, and 1.5. The refinements of the patterns of $La_2NiO_3F_2$ + xNaH with x = 0.25, 0.5, and 1.5 are given in Figures 4, 7, and 8, respectively (the refinements of $La_2NiO_3F_2$ + xNaH with x = 1 are given in Figure S5). Due to the presence of two to three reduced phases (beside side and decomposition products) within each sample, a structural model of a particular phase was deduced from the measurement, showing the highest phase fraction of this phase. The obtained model was then used in the refinement of the other samples with lower phase fractions of the phase. While doing so, no significant changes in structural parameters (lattice parameters, atom positions, site occupations, etc.) of the phase and stable convergence of the refinements were observed. Although structural characterization had to be performed on phase mixtures, the large d-spacing range covered with the measurement in combination with the changes of resolution of the diffraction detector banks and sufficient peak separation of the phases allows the determination of a concise picture of the structural changes that occur on the reductive fluoride extraction from $La_2NiO_3F_2$.

Facilitated by the high phase fraction of monoclinic $La_2NiO_3F_{2-a}$ (~73 wt %) within the sample, its structural model was derived from the measurement of $La_2NiO_3F_2$ + 0.25NaH (Figure 4). Indexing could be performed with a base-centered $\sqrt{2} \times \sqrt{2} \times 1$ supercell of the tetragonal aristotype RP-type structure. Different structural models were tested, and a close structural relationship between orthorhombic $La_2NiO_3F_2$ (space group: $Cccm$) and the monoclinic reduced phase $La_2NiO_3F_{2-a}$ was observed. Here, it is found that reduction of the symmetry from the orthorhombic space group $Cccm$ toward a monoclinic distortion with C centering is possible only for the translationengleiche subgroups $C12/m1$ or $C12/c1$, with superior fits obtained for the model with $C12/c1$ symmetry (for comparison, refined patterns with space group $C12/m1$ can be found in Figure S6). The corresponding symmetry tree and the refined structural parameters are given in Figure 5 and Table 2, respectively.

Oxide and fluoride ions are indistinguishable by neutron and X-ray diffraction due to the nearly identical scattering lengths and atomic form factors. Nevertheless, the neutron diffraction data can be used to investigate the structure and composition of the anion sublattice in more detail by analysis of the occupation factors of anion sites. The symmetry reduction from $I4/mmm$ to $C12/c1$ leads to a splitting of the interlayer anion site into two 4e crystallographic sites (Figure 5). Similar to what was found for $La_2NiO_3F_2$,[29] only one of those sites is fully occupied, resulting in a channel-like half-filling of the interstitial sites. When also refining the occupations of the equatorial and apical anion sites, a small but considerable decrease in the occupancy of the apical anion site is observed, while the equatorial anion site remains fully occupied. From this, an overall composition of approximately $La_2NiX_{4.93}$ or of $La_2NiO_3F_{1.93}$ (assuming that only fluoride is extracted in the reduction process) can be derived. Furthermore, this indicates that the fluoride is, as in $La_2NiO_3F_2$, occupying the apical anion site. Major structural rearrangements of the oxide and fluoride ions between different anion sites upon the reduction with low amounts of NaH can, therefore, be excluded. This can be confirmed by bond-valence-sum calculations where, similar to calculations made on $La_2NiO_3F_2$,[29] more stable configurations are found when fluoride is occupying the apical site. In comparison to the orthorhombic parent phase $La_2NiO_3F_2$, the slight reduction results in a change of the b/c ratio toward unity accompanied by the monoclinic distortion. For orthorhombic $La_2NiO_3F_2$, the distortion originates from a considerable tilting of the NiO_4F_2 octahedra along the b axis.[29] The additional degrees of freedom of the monoclinic compound also enable a tilting of the octahedra along the c axis. This tilting leads to an increase in the distance of F^{ap}−F^{ap} ($d(X2^a-X2^{ap})$ ($La_2NiO_3F_2$) = 2.88 Å, $d(X2^{ap}-X2^{ap})$ ($La_2NiO_3F_{2-a}$) = 2.93 Å) between two neighboring perovskite building blocks. As it will be shown in Section 3.1.2.2, this structural behavior on small extraction of fluoride ions can be well confirmed from DFT-based calculations on compounds with composition $La_2NiO_3F_{1.75}$ and will be explained there in

https://dx.doi.org/10.1021/acs.chemmater.0c00193
Chem. Mater. 2020, 32, 3160−3179

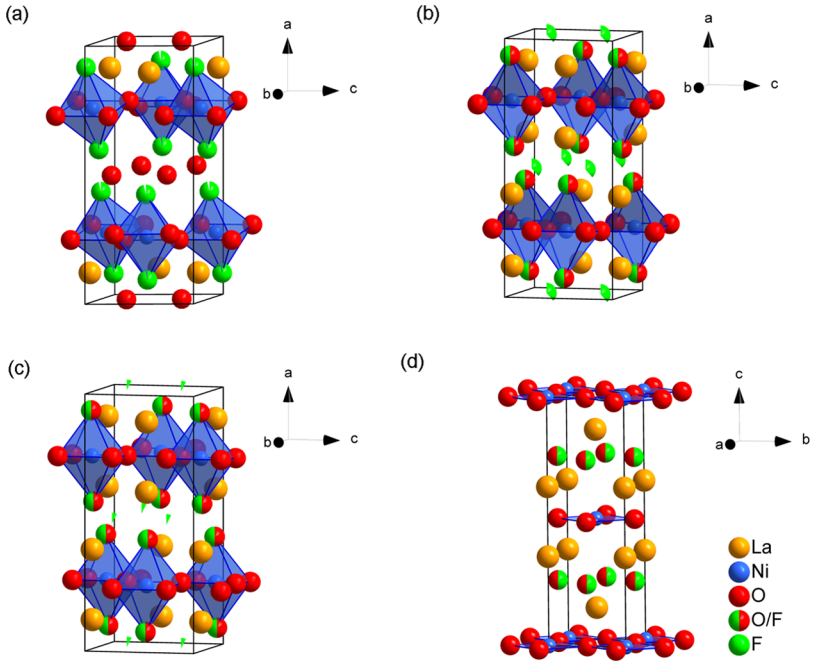

Figure 6. Crystal structure of monoclinic $La_2NiO_3F_{2-a}$ (approximate composition: $La_2NiO_3F_{1.93}$), (a) orthorhombic #1 $La_2NiO_3F_{2-b}$ (approximate composition: $La_2NiO_3F_{1.39}$), (b) orthorhombic #2 $La_2NiO_3F_{2-c}$ (approximate composition: $La_2NiO_3F_{1.08}$), (c) and tetragonal $La_2NiO_3F_{2-d}$ (approximate composition: La_2NiO_3F) (d). For mixed anion sites, a 0.5/0.5 O/F occupation was assumed.

detail. The crystal structure of $La_2NiO_3F_{2-a}$ is shown in Figure 6a.

In the sample $La_2NiO_3F_2$ + 0.25NaH, besides the main phase $La_2NiO_3F_{2-a}$, additionally, the phase $La_2NiO_3F_{2-b}$ (~14 wt %) is present. The structural model of $La_2NiO_3F_{2-b}$ was derived from the sample $La_2NiO_3F_2$ + xNaH with x = 0.5 (Figure 7), since this sample has a higher phase fraction of this phase. The highest weight fractions of $La_2NiO_3F_{2-c}$ (~45 wt %) and $La_2NiO_3F_{2-d}$ (~18 wt %) were found in the sample $La_2NiO_3F_2$ + 1.5NaH (Figure 8), and their structural models were derived from its measurement.

For both $La_2NiO_3F_{2-b}$ and $La_2NiO_3F_{2-c}$, best fits could be achieved using structural models with space group *Cccm*. Higher symmetries such as *Fmmm* or other orthorhombic space groups, which show different tilting patterns of the NiX_6 octahedra (e.g., *Cmce*[62]), were tested in addition. These models can, however, not explain the superstructure reflection at, e.g., $d \approx 5.1$ Å, which can be described using the *Cccm* model. The structural parameters are given in Tables 3 and 4.

When refining the occupations of the equatorial, apical, and interstitial sites of the orthorhombic phases, the occupation factor of the 4b interstitial site, which was fully occupied in $La_2NiO_3F_2$, decreases considerably, resulting in a composition of $La_2NiX_{4.39}$ ($La_2NiO_3F_{1.39}$) for orthorhombic #1 $La_2NiO_3F_{2-b}$ and of $La_2NiX_{4.08}$ ($La_2NiO_3F_{1.08}$) for orthorhombic #2 $La_2NiO_3F_{2-c}$. For monoclinic $La_2NiO_3F_{2-a}$, it was found that vacancies are formed on the apical sites, i.e., where the fluoride ions were located in the parent phase $La_2NiO_3F_2$. In contrast, no indication was given for the presence of vacancies on the apical sites for the orthorhombic phases $La_2NiO_3F_{2-b}$ and $La_2NiO_3F_{2-c}$. This shows that at least a partial rearrangement of anions between the apical and interstitial sites can take place, which is also accompanied by a lowering of the tilting of the NiX_6 polyhedra. This lowering of the tilting leads to a decrease of the bond valance sums of the interstitial anion site, which renders the allocation of fluoride ions on it more plausible. This correlates with a change in the bond distances of Ni to the apical ($X2^{ap}$) and equatorial ($X1^{eq}$) anions, showing increased stretching of the octahedra for increased amounts of used NaH (Table 5 and Figure 6b,c). This is in plausible agreement with the formation of Jahn−Teller active Ni^+ and is also observed for DFT-based calculations (see Section 3.1.2.2). Furthermore, when comparing the bond distances between apical ($X2^{ap}$) and interstitial anions ($X3^{int}b$) of $La_2NiO_3F_2$ and the reduced monoclinic and orthorhombic phases, it can be seen that the distances decrease considerably, indicating that the tilting of the octahedra decreases for stronger reduced phases. These distances are relatively short, but it has to be taken into account that the occupancies of this interstitial site in these phases decrease significantly. This also shows that refinements can only serve to determine an average structure of the disordered state, in which local adaptations have to be expected. The unrealistic small distances between the apical ($X2^{ap}$) and the unoccupied interstitial anions ($X3^{int}a$) highlight, moreover, that this interstitial site cannot be occupied. The distances between two apical sites ($X2^{ap}$) of neighboring perovskite building blocks are also given.

On the further increase in the amount of NaH, tetragonal $La_2NiO_3F_{2-d}$ (Figure 8) is formed. This phase was found to possess a completely different intensity pattern with strong changes in the relative reflection intensities compared to the T-related orthorhombic #1 and #2 phases $La_2NiO_3F_{2-b}$ and $La_2NiO_3F_{2-c}$ in the neutron diffraction pattern (see Figure S7 in the Supporting Information). This intensity pattern is indicative of the formation of a T′-type compound (space group *I*4/*mmm*), where the apical site is empty and the interstitial site is filled and, thus, resulting in square-planar coordination for the Ni cations (Figure 6d). The structural parameters are listed in Table 6. DFT calculations (see Section 3.1.2.2) support this observation, showing that this is the most stable structure for a composition of La_2NiO_3F. Such T′-type

https://dx.doi.org/10.1021/acs.chemmater.0c00193
Chem. Mater. 2020, 32, 3160−3179

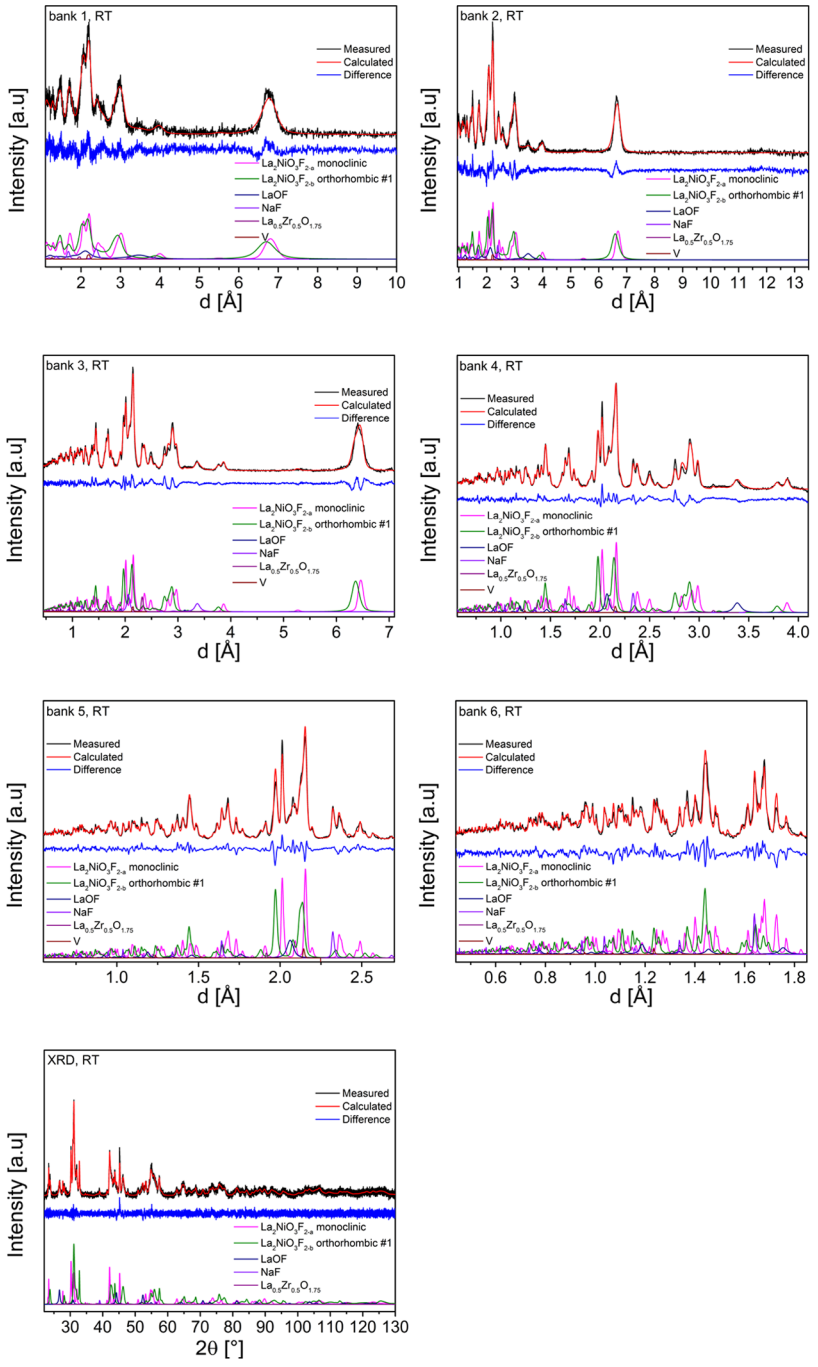

Figure 7. Coupled Rietveld analysis of $La_2NiO_3F_2$ + 0.5NaH of GEM bank 1−6 NPD and XRD data measured at room temperature (RT), from which the structural model of orthorhombic #1 $La_2NiO_3F_{2-b}$ (approximate composition: $La_2NiO_3F_{1.39}$) was derived.

RP phases have only been found for compounds containing high amounts of Jahn−Teller active cations, e.g., for the Nd_2CuO_4,[52] $La_3Ni_2O_6$,[25] and $La_4Ni_3O_8$,[2424] giving further support that a composition close to La_2NiO_3F is obtained here.[24,25,63]

3.1.2.2. Transmission Electron Microscopy Characterization. High-resolution TEM imaging can be a powerful technique to investigate structural changes in phase mixtures. However, this type of analysis is impeded by the fact that the crystals obtained are generally quite thick and can be composed of multiple domains of different RP-type phases as well as decomposition and side products. Therefore, an alternative approach was used to confirm the structures observed via X-ray and neutron powder diffraction methods by independent means using the Fast-ADT technique. This relatively new tool is based on the sequential acquisition of electron diffraction patterns from preferably monodomain crystals at different consecutive tilt angles, which are separated by a fixed tilt step. The three-dimensional (3D) reconstruction of this diffraction space data allows the determination of crystal structures in a similar way as single-crystal X-ray methods.

To reinforce the proposed structures of $La_2NiO_3F_2$ and the reduced phases derived from X-ray and neutron powder diffraction, Fast-ADT measurements were performed on $La_2NiO_3F_2$ and the reduction reaction products with 0.25 and 1.5NaH. The selection of suitable crystals for the

https://dx.doi.org/10.1021/acs.chemmater.0c00193
Chem. Mater. 2020, 32, 3160−3179

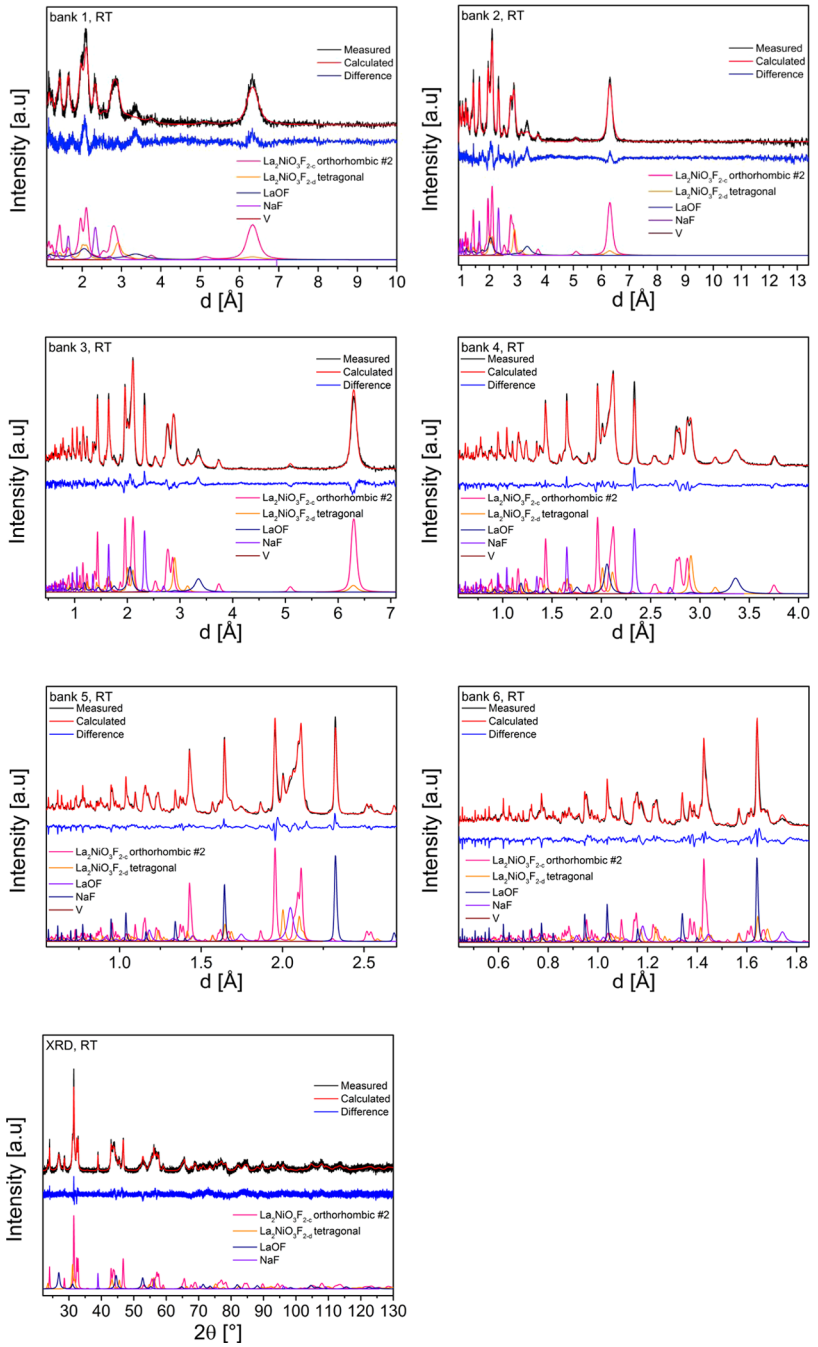

Figure 8. Coupled Rietveld analysis of $La_2NiO_3F_2$ + 1.5NaH of GEM bank 1−6 NPD and XRD data measured at room temperature (RT), from which the structural models of orthorhombic #2 $La_2NiO_3F_{2-c}$ (approximate composition: $La_2NiO_3F_{1.08}$) and tetragonal $La_2NiO_3F_{2-d}$ (approximate composition: La_2NiO_3F) were derived.

measurements had proven to be very difficult because they have to be reasonably thin to obtain good-quality data sets. Although thinner particles (see Figure S8 in the Supporting Information) were chosen for the acquisition of the Fast-ADT data, these crystals were still relatively thick for electron diffraction. Most of the analyzed particles contain twins, other domains, or large amounts of the side product NaF and/or the decomposition product LaOF for higher NaH amounts, which hamper successful structure determination of some of the reported phases. Furthermore, it cannot be excluded that a (partial) re-oxidation of the phases has taken place during the preparation of the samples; especially, isolated particles should be more prone toward oxidation. However, the deduction of unit-cell and space group information was possible for all measurements. The obtained lattice parameters (within the accuracy of this method) and space group information (see Table S2 in the Supporting Information) are in agreement with the results obtained from X-ray and neutron diffraction reported in the previous sections.

Using dynamical refinement approaches, it was possible to confirm the orthorhombic structure of the precursor material $La_2NiO_3F_2$ reported previously[29] and the monoclinic structure of $La_2NiO_3F_{2-a}$ present within the reduction reaction product with $x = 0.25$ (see Tables S3 and S4 in the Supporting Information). We also attempted to refine the structures of the orthorhombic #1 and #2 phases as well as the tetragonal phase

https://dx.doi.org/10.1021/acs.chemmater.0c00193
Chem. Mater. 2020, 32, 3160−3179

Table 3. Structural Parameters of Orthorhombic #1 $La_2NiO_3F_{2-b}$ (Approximate Composition: $La_2NiO_3F_{1.39}$) from Coupled Analysis of X-ray and Neutron Diffraction Data of $La_2NiO_3F_2$ + 0.5NaH

	Wyckoff site	x	y	z	occupancy	thermal displacement (Å^2)
La1	8l	0.1117(2)	0.7416(5)	0	1	0.73(1)
Ni1	4e	1/4	1/4	0	1	0.73(1)
O1 at X1^{eq}	8g	0.2430(4)	0	1/4	1	0.73(1)
O2/F1 at X2^{ap}	8l	0.9271(3)	0.8153(4)	0	1	0.73(1)
X3a^{int}	4a	0	0	1/4	0	0.73(1)
F2 at X3b^{int}	4b	0	1/2	1/4	0.386(9)	0.73(1)
a (Å)	12.698(1)		*b* (Å)	5.6484(5)		
c (Å)	5.4675(5)					
R_{wp}(XRD + NPD) (%)	4.44	GOF(XRD + NPD)	2.36	R_{bragg} (%)	0.34 (XRD)	
					1.65 (NPD, bank 3)	
space group	*Cccm*					

Table 4. Structural Parameters of Orthorhombic #2 $La_2NiO_3F_{2-c}$ (Approximate Composition: $La_2NiO_3F_{1.08}$) from Coupled Analysis of X-ray and Neutron Diffraction Data of $La_2NiO_3F_2$ + 1.5NaH

	Wyckoff site	x	y	z	occupancy	thermal displacement (Å^2)
La1	8l	0.1134(1)	0.7500(5)	0	1	0.44(1)
Ni1	4e	1/4	1/4	0	1	0.44(1)
O1 at X^{eq}	8g	0.2558(3)	0	1/4	1	0.44(1)
O2/F1 at X2^{ap}	8l	0.9284(2)	0.7875(3)	0	1	0.44(1)
X3a^{int}	4a	0	0	1/4	0	0.44(1)
F2 at X3b^{int}	4b	0	1/2	1/4	0.077(5)	0.44(1)
a (Å)	12.5309(3)		*b* (Å)	5.5427(1)		
c (Å)	5.4758(1)					
R_{wp}(XRD + NPD) (%)	4.31	GOF(XRD + NPD)	2.28	R_{bragg} (%)	1.35 (XRD)	
					2.46 (NPD, bank 3)	
space group	*Cccm*					

found in the products with x = 0.25 and 1.5. Although C-centered orthorhombic and tetragonal phases could be observed, accurate structural analyses of these phases were not possible. This is presumably due to an epitaxial growth of the decomposition product LaOF on the reduced RP-type phases along the *c* axis, which biases the obtained reflection intensities significantly. This epitaxy gives an indication of the decomposition mechanism of the metastable oxyfluoride phases, which will be discussed in a follow-up article. The phase fractions of LaOF increase, moreover, significantly for higher NaH contents (Figure 5c). Therefore, it is not possible to confirm the structural models of the stronger reduced phase determined from coupled Rietveld analysis of X-ray and neutron diffraction data by means of electron diffraction methods.

It has to be pointed out that the combination of X-ray and neutron diffraction methods provides a more robust analysis of the anion sublattice, especially with respect to small details in anion occupancies found for $La_2NiO_3F_2$ and $La_2NiO_3F_{2-a}$.

3.1.2.3. DFT Calculations: Toward Understanding the Structural Distortions in Reduced Phases. As shown in the previous section, a complete structural understanding of the anion chemistry of the compounds is difficult to achieve experimentally. Therefore, DFT calculations were performed to develop a deeper understanding of the most favorable structural relaxations of the anion sublattice on reductive defluorination of $La_2NiO_3F_2$. To do so, the orthorhombic structural model of $La_2NiO_3F_2$ (*Cccm*, as published in ref 29) was considered as a starting point. Then, one to four fluoride ions per unit cell were subsequently removed (corresponding to compositions of $La_2NiO_3F_{1.75}$ to La_2NiO_3F), and the structure was allowed to relax. In addition, various different relative orientations of the introduced vacancies were examined together with different distributions of oxide and fluoride ions at the apical and/or interstitial sites. The equatorial site was always occupied by oxide ions. In the following, the discussion is limited to the changes of the initial to the most stable relaxed structures of the reduced phases.

For calculations on compounds $La_2NiO_3F_{2-\Delta}$ with high values of Δ, it was found that the remaining anions show a very high mobility, although no molecular dynamics was chosen (i.e., a structural optimization at 0 K). This is exemplified for the defluorinated compound with composition La_2NiO_3F (Figure 9). For this compound, a complete relaxation to the T′ structure can be observed for suitable initial vacancy configurations, which results from the movement of apical fluoride ions to the interstitial site, leading to a fully unoccupied apical site and a fully occupied interstitial site (an occupation with 50% F^- and 50% O^{2-} is assumed). This is in agreement with the experimental observation of a tetragonal T′-type $La_2NiO_3F_{2-d}$ phase (see Section 3.1.2). It was found that the principle relaxation of the lattice parameters on transition to the T′-type structure could also be reproduced: the *b* and *c* lattice parameters after relaxation are found to be on the order of 5.7−5.8 Å, which is close to the experimental value 5.65 Å, whereas the lattice parameter *a* decreases to 12.67 Å (12.52 Å experimentally). Furthermore, it was found that a relaxation to the T′ structure is independent of the initial anion configuration; both $La_2Ni(O_2)^{eq}(F)^{ap}(O)^{int}$ and $La_2Ni(O_2)^{eq}(O)^{ap}(F)^{int}$ relax to T′-type $La_2Ni(O_2)^{eq}(\square)^{ap}(OF)^{int}$.

https://dx.doi.org/10.1021/acs.chemmater.0c00193
Chem. Mater. 2020, 32, 3160−3179

Table 5. Bond Distances of $La_2NiO_3F_2$, Monoclinic $La_2NiO_3F_{2-a}$, Orthorhombic #1 $La_2NiO_3F_{2-b}$, Orthorhombic #2 $La_2NiO_3F_{2-c}$, and Tetragonal $La_2NiO_3F_{2-d}$[a]

	bond distance (Å)				
	$La_2NiO_3F_2$	$La_2NiO_3F_{2-a}$ monoclinic	$La_2NiO_3F_{2-b}$ orthorhombic #1	$La_2NiO_3F_{2-c}$ orthorhombic #2	$La_2NiO_3F_{2-d}$ tetragonal
La1−$X1^{eq}$	2.539(2) [2×]	2.423(2) [1×]	2.552(4) [2×]	2.546(3) [2×]	2.665(2) [4×]
	2.813(2) [2×]	2.621(2) [1×]	2.721(4) [2×]	2.642(3) [2×]	
		2.626(2) [1×]			
		3.145(2) [1×]			
La1−$X2^{ap}$	2.356(2) [1×]	2.379(2)	2.551(4) [1×]	2.617(3) [1×]	
	2.602(2) [1×]	2.577(2)	2.809(1) [2×]	2.7953(6) [2×]	
	2.809(1) [2×]	3.176(2)	3.184(4) [1×]	3.025(3) [1×]	
		3.450(2)			
La1−$X3b_{Cccm\ or\ C1_2/c1}{}^{int}$ or La1−$X3_{I4/mmm}{}^{int}$	2.4718(8) [2×]	2.486(2)	2.396(2) [2×]	2.411(2) [2×]	2.417(1) [4×]
		2.487(2)			
Ni1−$X1^{eq}$	2.0076(2) [4×]	2.071(2) [2×]	1.9673(3) [4×]	1.9492(1) [4×]	1.9962(1) [4×]
		2.019(2) [2×]			
Ni1−$X2^{ap}$	2.160(2) [2×]	2.152(3) [2×]	2.279(4) [2×]	2.245(3) [2×]	
$X2^{ap}$−$X3a_{Cccm\ or\ C1_2/c1}{}^{int}$ or $X2^{ap}$−$X3_{I4/mmm}{}^{int}$	1.990(2) [2×]	1.876(1) [1×]	1.953(2) [2×]	2.017(2) [2×]	2.2921(1) [4×]
		2.174(2) [1×]			
	($X3^{int}a_{Cccm}$ is unoccupied)	($X3^{int}a_{C1_2/c1}$ is unoccupied)	($X3^{int}a_{Cccm}$ is unoccupied)	($X3^{int}a_{Cccm}$ is unoccupied)	($X2^{ap}$ is unoccupied)
$X2^{ap}$−$X3b_{Cccm\ or\ C1_2/c1}{}^{int}$ or $X2^{ap}$−$X3_{I4/mmm}{}^{int}$	2.657(2) [2×]	2.659(3) [1×]	2.428(2) [2×]	2.284(2) [2×]	
		2.733(2) [1×]			
$X2^{ap}$−$X2^{ap}$	2.883(2) [1×]	2.933(2) [1×]	2.790(5) [1×]	2.961(3) [1×]	3.6117(1) [4×]
	3.536(2) [2×]	3.297(2) [1×]	3.302(3) [1×]	3.274(2) [1×]	
	4.552(3) [1×]	3.963(2) [1×]	4.014(4) [2×]	3.658(2) [2×]	($X2^{ap}$ is unoccupied)
		4.599(2) [1×]			

[a] $X1^{eq}$ refers to the equatorial, $X2^{ap}$ to the apical, and $X3^{int}$ to the interstitial anion site. In the orthorhombic space group *Cccm* of $La_2NiO_3F_2$, $La_2NiO_3F_{2-b}$, and $La_2NiO_3F_{2-c}$ and in the monoclinic space group *C*12/*c*1 of $La_2NiO_3F_{2-b}$, two interstitial anion sites $X3^{int}a_{Cccm\ or\ C1_2/c1}$ and $X3^{int}b_{Cccm\ or\ C1_2/c1}$ exist, of which only $X3^{int}b_{Cccm\ or\ C1_2/c1}$ is (partially) occupied. The tetragonal space group *I*4/*mmm* of $La_2NiO_3F_{2-d}$ has just one interstitial site $X3_{I4/mmm}{}^{int}$. $X2^{ap}$ of the $La_2NiO_3F_{2-d}$ is unoccupied.

Table 6. Structural Parameters of $La_2NiO_3F_{2-d}$ (Approximate Composition: La_2NiO_3F) from Coupled Analysis of X-ray and Neutron Diffraction Data of $La_2NiO_3F_2$ + 1.5NaH

	Wyckoff site	*x*	*y*	*z*	occupancy	thermal displacement (Å^2)
La1	4e	0	0	0.6411(2)	1	0.44(1)
Ni1	2a	0	0	0	1	0.44(1)
O1 at X^{eq}	4c	0	1/2	0	1	0.44(1)
$X2^{ap}$	4e	0	0	0.84	0	0.44(1)
O2/F1 at $X3a^{int}$	4d	0	1/2	1/4	1	0.44(1)
a (Å)	3.9925(2) ($a^*\sqrt{2}$ = 5.6462(3))	*c* (Å)	12.5150(9)			
R_{wp}(XRD + NPD) (%)	4.31	GOF(XRD + NPD)	2.28	R_{bragg} (%)	0.77 (XRD) 1.85 (NPD, bank 3)	
space group	*I*4/*mmm*					

We would also like to emphasize that a relaxation to a T′-type structure seems to be hindered if the relative locations of the vacancies toward each other are unfavorable (Figure 9). This might also explain why both T- and T′-type compounds can be observed for the defluorination of $La_2NiO_3F_2$. This behavior is in principle also found for intermediate compositions, such as $La_2NiO_3F_{1.25}$ and $La_2NiO_3F_{1.5}$.

Removing only one fluoride ion from the unit cell of $La_2NiO_3F_2$ results in a composition of $La_2NiO_3F_{1.75}$. With respect to the subgroups of *Cccm*, this corresponds to a monoclinic ordering variant (isomorphic subgroups that maintain the orthorhombic symmetry for a similar composition require a 3- to 5-fold increase of the unit-cell size, which was computationally too costly to be considered). This deviation from the orthorhombic symmetry is also found in a partly relaxed structure (compare Figure 10, right (i) and (ii)), where the angle γ changes due to this artificial fluoride ion/vacancy ordering. On fully relaxing the structure by inducing further strain, it is found that the energetically most stable structure has a similar distortion and tilting pattern as the experimentally found structure of the monoclinic compound $La_2NiO_3F_{1.93}$ (compare Figure 10, right (iii) and (iv)), which is expressed by the deviation of the angle β from 90°. The structural distortion is complicated and can be explained as follows: the reductive defluorination results in a change of the electronic structure to a d^9 Jahn−Teller-active electron configuration of the formed Ni^+. This Ni^+ ion is located in the NiO_4F polyhedron and, consequently, close to the anion vacancy. The polyhedron

https://dx.doi.org/10.1021/acs.chemmater.0c00193
Chem. Mater. 2020, 32, 3160−3179

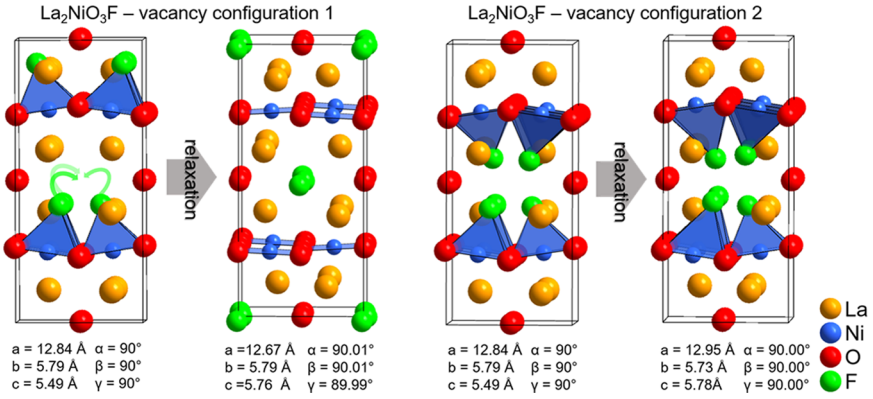

Figure 9. Structural relaxation of different vacancy-ordered starting models of La_2NiO_3F. The starting models were derived based on removing fluoride ions from the experimentally determined orthorhombic structure of $La_2NiO_3F_2$.[2929] Configuration 1 was found to relax to a T′-type structure, whereas configuration 2 does not.

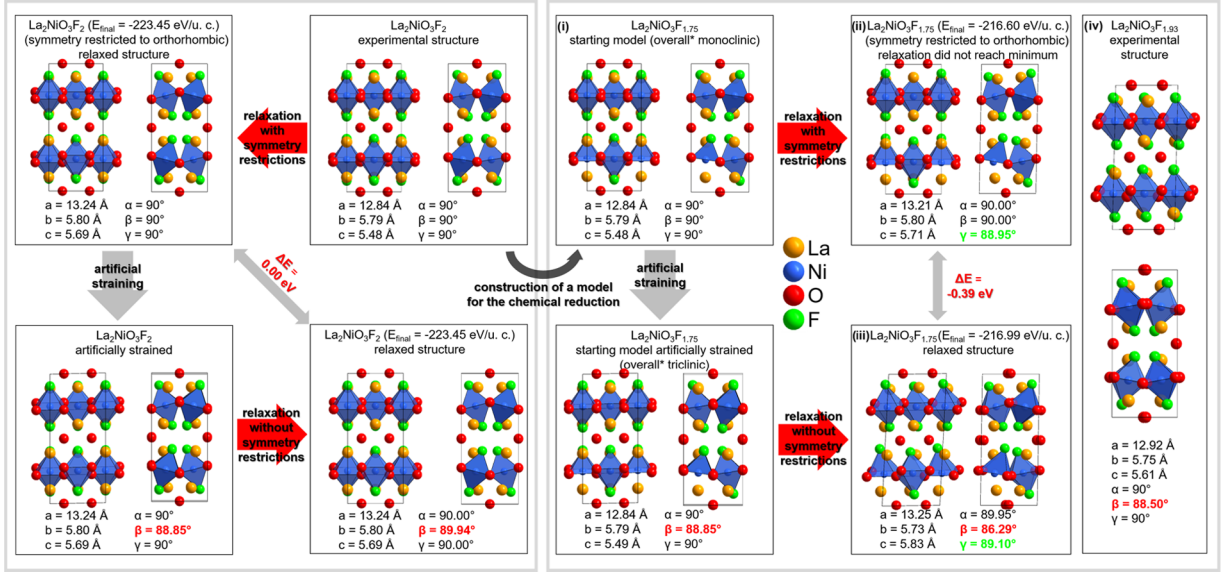

Figure 10. Scheme of the DFT-based calculations performed to determine the most stable structure for chemically reduced $La_2NiO_3F_{1.93}$ by performing calculations on strained and nonstrained $La_2NiO_3F_2$ (left) and $La_2NiO_3F_{1.75}$ (right). *: "Overall" refers to the combination of cell metrics and inner symmetry of the atoms. The viewing directions of the left (upper) and right (lower) representations corresponding to one relaxed structure are along the *b* axis and *c* axis, respectively.

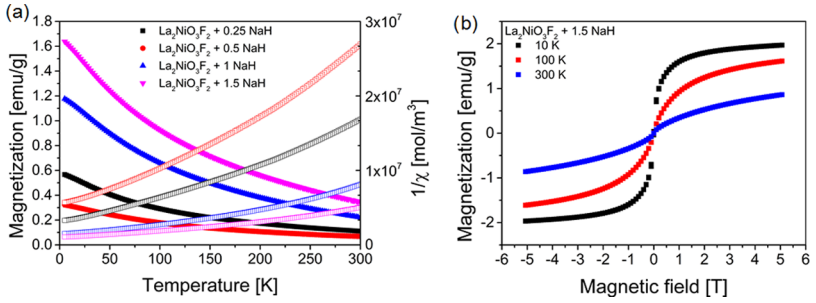

Figure 11. (a) Magnetization vs temperature curves of $La_2NiO_3F_2$ + *x*NaH measured at $\mu_0 H$ = 1 T (filled symbols, FC and ZFC curves overlap) and inverse susceptibility vs temperature curves of $La_2NiO_3F_2$ + *x*NaH with *x* = 0.25, 0.5, 1, and 1.5 (open symbols); (b) magnetization vs magnetic field curves of $La_2NiO_3F_2$ + 1.5NaH measured at 10, 100, and 300 K. Measurements of $La_2NiO_3F_2$ + *x*NaH with *x* = 0.25, 0.5, and 1 can be found in Figure S9.

distorts toward square-planar coordination by shifting the remaining fluoride ion away from the apical site toward the position of the interstitial site. However, this shift is energetically costly due to the proximity to the fluoride ion of the polyhedron with identical tilting in the layer above. By inducing the tilting along the *c* axis, the fluoride ion of the NiO_4F polyhedron can move further away from the central Ni ion by an additional ~0.12 Å = $\Delta(d_{Ni-F}) = d_{Ni-F,}$Figure

https://dx.doi.org/10.1021/acs.chemmater.0c00193
Chem. Mater. 2020, 32, 3160−3179

$10_{(right)(iii)} - d_{Ni-F,}$Figure $10_{(right)(ii)}$, while additionally increasing the distance to the next closest fluoride ion by ∼0.05 Å. This has a strong, energetic impact of −0.39 eV per unit cell (u.c.).

The electronic origin of the monoclinic distortion can also be verified by comparing with results of a similar calculation strategy for the structure of $La_2NiO_3F_2$. Even after inducing a monoclinic strain to $La_2NiO_3F_2$, a relaxation back to the orthorhombic symmetry with negligible orthorhombic distortion (β = 89.94°) and energy difference (0.00 eV per unit cell) can be observed (Figure 10, left). This indicates the absence of a structural driving force for lowering the symmetry in stoichiometric, well-ordered $La_2NiO_3F_2$, highlighting the strong impact of small compositional changes in materials containing elements with d^9 electron configuration.

3.1.3. Magnetic Characterization of $La_2NiO_3F_2$ and Its Reduction Products. 3.1.3.1. SQUID Measurements. In our previous work,[29] it was shown that $La_2NiO_3F_2$ orders magnetically below 49 K, where the low magnitude of the magnetic moment indicates an antiferromagnetic ordering.

The reduction reaction products $La_2NiO_3F_2$ + xNaH with x = 0.25, 0.5, 1, and 1.5 were characterized by ZFC/FC measurements in the temperature range from 5 to 300 K (Figure 11a). No divergence in magnetization between ZFC and FC measurements was observed. The overall magnetization increases strongly for samples where higher amounts of NaH were used in the reduction. This provides an indication for a magnetic contribution of a decomposition product to the otherwise antiferromagnetic or paramagnetic phases formed upon the reduction of $La_2NiO_3F_2$ (see Section 3.1.3.2). Due to a weak hysteresis in field-dependent measurements (Figure 11b), the presence of a ferromagnetic component can be assumed. The analysis of the reaction mechanism (see Section 3.1.1) suggests that the ferromagnetic contribution originates from metallic Ni, which is formed due to the strong decomposition of $La_2NiO_3F_2$ during the defluorination process. In accordance with previous findings made on the reduction of $LaNiO_3$ to $LaNiO_2$,[22] the Ni seems to be amorphous or nanocrystalline and, hence, its presence cannot by confirmed by diffraction experiments only (see Section 3.1.1). Overall, the magnetic measurements on their own cannot reveal changes in the magnetic properties of the parent $La_2NiO_3F_2$ phase on reduction.

3.1.3.2. Determination of Magnetic Structures. To develop a deeper understanding of the magnetic properties of the phases after reduction, neutron diffraction data were recorded at low temperatures. The comparison between data measured at room temperature and at 10 K (Figure 12) shows the appearance of additional reflections in all reduction reaction products. Since Ni^+ and Ni^{2+} ions do not possess a large spin moment, the intensity of the magnetic reflections is low; thus, only two reflections can be clearly observed.

For the orthorhombic parent sample $La_2NiO_3F_2$ and the reduced samples $La_2NiO_3F_2$ + xNaH with x = 0.25 and 0.5, the additional reflections could be indexed with a k-vector of [100] based on the nuclear structures determined in Section 3.1.2. The magnetic reflections in $La_2NiO_3F_2$ + xNaH with x = 0.25 and 0.5 can be attributed to the reduced monoclinic phase $La_2NiO_3F_{2-a}$ with an approximate composition of $La_2NiO_3F_{1.93}$. Since the number of additional reflections is low, the amount of additional refinement parameters was limited using a magnetic subgroup approach, i.e., refining the magnetic intensities within one of the maximal magnetic

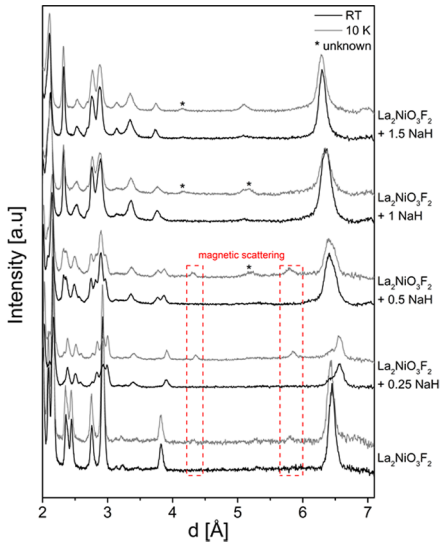

Figure 12. Comparison between GEM bank 3 NPD data measured at room temperature (RT) and 10 K of $La_2NiO_3F_2$ and $La_2NiO_3F_2$ + xNaH with x = 0.25, 0.5, 1, and 1.5. Reflections attributed to magnetic scattering are highlighted. Reflections that could not be identified are marked with *.

subgroups of the nuclear structures.[64] By this approach, it is possible to limit the additional refinement parameters to a single parameter. This is due to the fact that the magnetic space group implies certain relative orientations of the magnetic moments of the Ni atoms. Robust refinements could be achieved based on the subgroups of the space groups *Cccm* and C12/*c*1 with a magnetic k-vector of [100], and good fits (Figure 13) could be obtained in the magnetic space groups $C_Pc'cm$ (66.9.572) and P_C2_1/c (14.84), with the magnetic vectors of the Ni ions aligning parallel to the c axis with G-type antiferromagnetic (AFM) ordering of the magnetic moments within the perovskite building blocks. The corresponding magnetic structures are shown in Figure 14a,b. It is also worth emphasizing that this inter- and intralayer ordering of magnetic moments was in principle also found for La_2NiO_4 and the stronger reduced n = 3 $La_4Ni_3O_8$ (67% Ni^+) by DFT-based calculations.[65]

Remarkably, at 10 K, strong differences are observed for the magnitudes of the magnetic moments refined for $La_2NiO_3F_2$ and for $La_2NiO_3F_{1.93}$ of 0.7(1) μ_B and 1.62(7) μ_B, respectively. This is surprising, since it would be assumed that a higher magnetic moment (2.83 μ_B for Ni^{2+} (d^8), 1.73 μ_B for Ni^+ (d^9)) would be found, the more Ni^{2+} would be present in the compound. It is known that superexchange interactions between adjacent layers are weak, and especially for the layered perovskite-related compounds of the n = 1 RP structure family A_2BO_4 with quasi-two-dimensional B−O−B networks, highly anisotropic magnetic interactions can be expected.[32−34] Furthermore, superexchange interactions via fluoride ions are weaker as compared to via oxide ions.[35]

In this respect, a comparison of the magnetic properties and structures to the system of the La_2NiO_{4+d} is also interesting. In La_2NiO_{4+d}, only the stoichiometric samples with d = 0 are reported to possess 3D antiferromagnetic ordering up to temperatures of 300 K,[62] while slightly overstoichiometric compounds (d > 0) show considerably lower transition temperatures.[66] For $La_2NiO_3F_2$, where the oxidation state is maintained with regard to La_2NiO_4, no 3D AFM ordering is

https://dx.doi.org/10.1021/acs.chemmater.0c00193
Chem. Mater. 2020, 32, 3160−3179

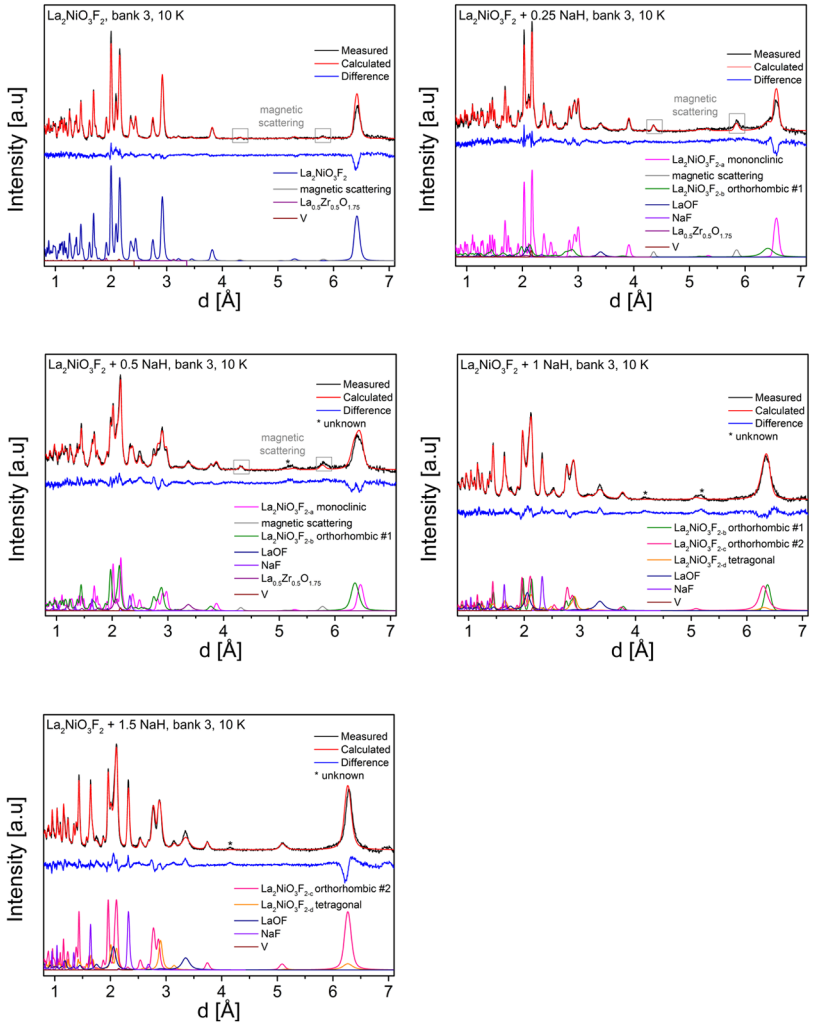

Figure 13. Rietveld analysis of magnetic structures of $La_2NiO_3F_2$ and $La_2NiO_3F_2$ + xNaH with x = 0.25, 0.5, 1, and 1.5 of GEM bank 3 NPD data measured at 10 K.

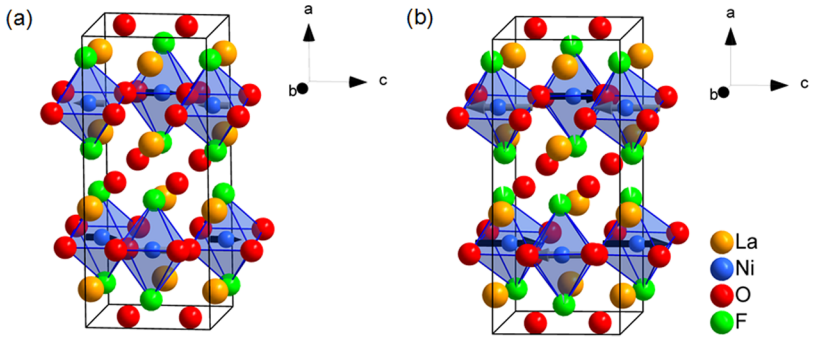

Figure 14. Magnetic structures of (a) $La_2NiO_3F_2$ and (b) $La_2NiO_3F_{2-d}$ at 10 K. Arrows indicate the length of the magnetic vectors as obtained from the refinement of neutron diffraction data.

present at ambient temperature,[29] and the moments found at 10 K are significantly lower than the moment of La_2NiO_4 of 1.68 μ_B (measured at 4 K).[62] This highlights that the introduction of additional anions into the interstitial site weakens magnetic interactions between adjacent layers. For $La_2NiO_3F_{1.93}$, ordering is found at least at up to 100 K without a significant decrease in the magnetic moment compared to lower temperatures (Figure 15). Furthermore, the moment is close to the moment found for La_2NiO_4 at 4 K. For monoclinically distorted $La_2NiO_3F_{1.93}$, it appears that the structural distortion in combination with the change of the electron configuration strengthens the exchange between adjacent perovskite building blocks. This might be explained by the fact that the Ni−F−F−Ni super-superexchange, found in $La_2NiO_3F_2$ only, is partly replaced by Ni−F−Ni super-exchange interactions, resulting in a strengthening of the 3D AFM interactions (Figure 15).

https://dx.doi.org/10.1021/acs.chemmater.0c00193
Chem. Mater. 2020, 32, 3160−3179

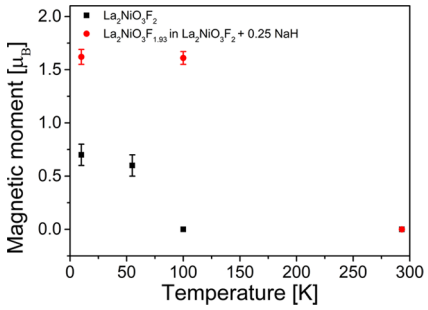

Figure 15. Magnetic moments as a function of the measurement temperature of $La_2NiO_3F_2$ and $La_2NiO_3F_{1.93}$ in $La_2NiO_3F_2$ + xNaH with x = 0.25. For $La_2NiO_3F_2$, FC and ZFC measurements showed a Néel temperature of 49 K[29]; however, the neutron powder diffraction data suggests a higher transition temperature (>55 K); the exact Néel temperature could, however, not be determined.

We would like to emphasize that it was not possible to draw robust and reliable conclusions about the magnetic properties and/or ordering scenarios for the stronger reduced phases. Even though additional reflections (marked with *) are present in the samples $La_2NiO_3F_2$ + xNaH with x = 0.5, 1, and 1.5 (Figures 12 and 13), they could not be indexed successfully by testing different $n \times m \times l$ superstructures with reasonably small n, m, $l \in \mathbb{N}$. Their analysis is impeded by the small number of identifiable reflections with low intensities, which show in one case overlapping with one neighboring nuclear reflection of another phase. The absence of these additional reflections in the ambient temperature measurements renders possible that they belong to a magnetic ordering process. However, a clear assignment would require that the higher reduced phases could be prepared in a phase purer state. With respect to the fact that no long-range magnetic ordering could be induced into the stronger reduced phases and $La_3Ni_2O_6$[25] and $La_4Ni_3O_8$,[24] this opens up exploratory space for future studies.

4. CONCLUSIONS

In this article, we have shown that the selective extraction of fluoride ions from $La_2NiO_3F_2$ can result in the formation of the first single-layer T′-type compound La_2NiO_3F derived from n = 1 RP-type $La_2NiO_3F_2$ containing only Ni as the transition-metal cation. In comparison to the reduction of the pure oxides, this is facilitated by the high anion content of the starting material $La_2NiO_3F_2$, which can be considered key for the formation of T′-type compounds, which do not tend to allow for overall anion contents y in A_2BX_y with $y < 4$.

On reductive defluorination of $La_2NiO_3F_2$, the structural changes are complex and can be understood with the aid of DFT-based calculations, showing the strong impact of the introduction of even small amounts of d^9-configured Ni^+ cations on structural distortions. These distortions were found to play a key role in inducing long-range magnetic ordering in partly reduced monoclinic $La_2NiO_3F_{1.93}$ by increasing the strength of the Ni−X−X−Ni superexchange interactions between adjacent perovskite building blocks. Furthermore, also the higher reduced compounds show small indications for the presence of long-range magnetic ordering, although their magnetic structure could not be determined.

Clearly, this article has shown that the defluorination of $La_2NiO_3F_2$ can provide a synthetic pathway for new magnetic materials, which cannot be obtained from the pure oxides easily. In a follow-up article, we will show that recently developed fluoride-ion batteries[67−71] can also serve as a means to obtain such compounds with low-valent Ni species.

■ ASSOCIATED CONTENT

Supporting Information

The Supporting Information is available free of charge at https://pubs.acs.org/doi/10.1021/acs.chemmater.0c00193.

Quantitative analysis and refined lattice parameters and unit-cell volumes of room-temperature XRD data of $La_2NiO_3F_2$ and reduction reaction products $La_2NiO_3F_2$ + xNaH ($0.25 \leq x \leq 2.5$); Rietveld refinements of XRD data measured at room temperature of $La_2NiO_3F_2$ and reduction reaction products $La_2NiO_3F_2$ + xNaH ($0.25 \leq x \leq 2.5$); comparison of the selected angular range of $La_2NiO_3F_2$ + 2.5NaH, indicating the presence of amorphous or nanocrystalline Ni; Rietveld refinements of XRD data of re-oxidized reduction reaction products $La_2NiO_3F_2$ + xNaH with x = 0.5, 1, and 1.5; X-ray diffraction patterns of reduction reaction products $La_2NiO_3F_2$ + xNaH with x = 1 and 1.5 after being exposed to F_2 gas for 15 min at various temperatures; coupled Rietveld refinements of $La_2NiO_3F_2$ +1 NaH of GEM bank 1−6 NPD and XRD data measured at room temperature; coupled Rietveld refinements of $La_2NiO_3F_2$ + 0.25NaH of GEM bank 1−6 NPD and XRD data measured at room temperature using a model with the space group $C1_2/m1$ for the monoclinic phase $La_2NiO_3F_{2-a}$; comparison between refined diffraction patterns of orthorhombic #2 $La_2NiO_3F_{2-c}$ (T-type structure) and tetragonal $La_2NiO_3F_{2-d}$ (T′-type structure) in $La_2NiO_3F_2$ + xNaH with x = 1.5 of GEM bank 3 and 4 NPD data measured at room temperature; high-angle annular dark-field (HAADF) images of measured crystals; unit-cell parameters of $La_2NiO_3F_2$ and phases within the reduction reaction products $La_2NiO_3F_2$ + xNaH with x = 0.25 and 1.5 determined from Fast-ADT measurements; atomic positions of structural models refined from Fast-ADT measurements by the dynamical approach in the Jana2006 program; data acquisition, structure solution, and dynamical refinement parameters of the crystals used for structure determination; and magnetization vs magnetic field curve of $La_2NiO_3F_2$ + xNaH with x = 0.25, 0.5, 1, and 1.5 measured at 10, 100, and 300 K (PDF)

■ AUTHOR INFORMATION

Corresponding Author

Oliver Clemens − *Fachgebiet Materialdesign durch Synthese, Institut für Materialwissenschaft, Technical University of Darmstadt, 64287 Darmstadt, Germany; Institute for Nanotechnology, Karlsruhe Institute of Technology, 73644 Eggenstein-Leopoldshafen, Germany;* orcid.org/0000-0002-0860-0911; Email: oliver.clemens@md.tu-darmstadt.de; Fax: +49 6151 16 20965

Authors

Kerstin Wissel − *Fachgebiet Materialdesign durch Synthese, Institut für Materialwissenschaft, Technical University of Darmstadt, 64287 Darmstadt, Germany;* orcid.org/0000-0003-4418-0595

https://dx.doi.org/10.1021/acs.chemmater.0c00193
Chem. Mater. 2020, 32, 3160−3179

Ali Muhammad Malik − *Fachgebiet Materialdesign durch Synthese, Institut für Materialwissenschaft and Fachgebiet Materialmodellierung, Institut für Materialwissenschaft, Technical University of Darmstadt, 64287 Darmstadt, Germany*

Sami Vasala − *Fachgebiet Materialdesign durch Synthese, Institut für Materialwissenschaft, Technical University of Darmstadt, 64287 Darmstadt, Germany*

Sergi Plana-Ruiz − *Fachgebiet Elektronenkristallographie, Institut für Angewandte Geowissenschaften, Technical University of Darmstadt, 64287 Darmstadt, Germany; LENS-MIND, Departament d'Enginyeria Electrònica i Biomèdica, Universitat de Barcelona, 08028 Barcelona, Catalonia*

Ute Kolb − *Fachgebiet Elektronenkristallographie, Institut für Angewandte Geowissenschaften, Technical University of Darmstadt, 64287 Darmstadt, Germany; Institut für Anorganische Chemie und Analytische Chemie, Centre for High Resolution Electron Microscopy, Johannes Gutenberg-Universität Mainz, 55128 Mainz, Germany*

Peter R. Slater − *School of Chemistry, University of Birmingham, Birmingham B15 2TT, United Kingdom*

Ivan da Silva − *ISIS Facility, Rutherford Appleton Laboratory, Didcot, Oxfordshire OX11 0QX, United Kingdom*

Lambert Alff − *Fachgebiet Dünne Schichten, Institut für Materialwissenschaft, Technical University of Darmstadt, 64287 Darmstadt, Germany*

Jochen Rohrer − *Fachgebiet Materialmodellierung, Institut für Materialwissenschaft, Technical University of Darmstadt, 64287 Darmstadt, Germany*

Complete contact information is available at: https://pubs.acs.org/10.1021/acs.chemmater.0c00193

Notes

The authors declare no competing financial interest.

■ ACKNOWLEDGMENTS

This work was funded by the German Research Foundation within the Emmy Noether program (grant no. CL551/2-1). K.W. acknowledges funding from the JUICED Hub (EPSRC grant no. EP/R023662/1) researcher mobility fund. Neutron diffraction beam time on GEM at ISIS was provided by the Science and Technology Facilities Council (STFC) (grant no. RB1820423).

■ REFERENCES

(1) Sanjaya Ranmohotti, K. G.; Josepha, E.; Choi, J.; Zhang, J.; Wiley, J. B. Topochemical Manipulation of Perovskites: Low-Temperature Reaction Strategies for Directing Structure and Properties. *Adv. Mater.* **2011**, *23*, 442−460.

(2) Slater, P.; Driscoll, L. Modification of Magnetic and Electronic Properties, in Particular Superconductivity, by Low Temperature Insertion of Fluorine into Oxides. *Photonic Electron. Prop. Fluoride Mater.* **2016**, *1*, 401−421.

(3) Greaves, C.; Francesconi, M. G. Fluorine insertion in inorganic materials. *Curr. Opin. Solid State Mater. Sci.* **1998**, *3*, 132−136.

(4) McCabe, E. E.; Greaves, C. Review: Fluorine insertion reactions into pre-formed metal oxides. *J. Fluorine Chem.* **2007**, *128*, 448−458.

(5) Clemens, O.; Slater, P. R. Topochemical modifications of mixed metal oxide compounds by low-temperature fluorination routes. *Rev. Inorg. Chem.* **2013**, *33*, 105−117.

(6) Slater, P. R. Poly(vinylidene fluoride) as a reagent for the synthesis of K_2NiF_4-related inorganic oxide fluorides. *J. Fluorine Chem.* **2002**, *117*, 43−45.

(7) Slater, P. R.; Gover, R. K. B. Synthesis and structure of the new oxide fluoride $Sr_2TiO_3F_2$ from the low temperature fluorination of Sr_2TiO_4: an example of a staged fluorine substitution/insertion reaction. *J. Mater. Chem.* **2002**, *12*, 291−294.

(8) Berry, F. J.; Ren, X.; Heap, R.; Slater, P.; Thomas, M. F. Fluorination of perovskite-related $SrFeO_{3-\delta}$. *Solid State Commun.* **2005**, *134*, 621−624.

(9) Yamamoto, T.; Kageyama, H. Hydride Reductions of Transition Metal Oxides. *Chem. Lett.* **2013**, *42*, 946−953.

(10) Bednorz, J. G.; Müller, K. A. Possible highT c superconductivity in the Ba-La-Cu-O system. *Z. Phys. B: Condens. Matter* **1986**, *64*, 189−193.

(11) Cava, R. J.; Batlogg, B.; Chen, C. H.; Rietman, E. A.; Zahurak, S. M.; Werder, D. Oxygen stoichiometry, superconductivity and normal-state properties of $YBa_2Cu_3O_{7-\delta}$. *Nature* **1987**, *329*, 423−425.

(12) Chevalier, B.; Tressaud, A.; Lepine, B.; Amine, K.; Dance, J. M.; Lozano, L.; Hickey, E.; Etourneau, J. Stabilization of a New Superconducting Phase by Low-Temperature Fluorination of La_2CuO_4. *Phys. C* **1990**, *167*, 97−101.

(13) Chu, C. W.; Hor, P. H.; Meng, R. L.; Gao, L.; Huang, Z. J.; Wang a, Y. Evidence for superconductivity above 40 K in the La-Ba-Cu-O compound system. *Phys. Rev. Lett.* **1987**, *58*, 405−407.

(14) Demazeau, G.; Tresse, F.; Plante, T.; Chevalier, B.; Etourneau, J.; Michel, C.; Hervieu, M.; Raveau, B.; Lejay, P.; Sulpice, A.; Tournier, R. Evolution of the Superconducting Properties in the La_2CuO_4 Lattice Versus Oxygen-Pressure. *Phys. C* **1988**, *153*, 824−825.

(15) MacManus, J. L.; Fray, D. J.; Evetts, J. E. Fluorination of $Y_1Ba_2Cu_3O_{7-x}$ by a solid state electrochemical method. *Phys. C* **1991**, *184*, 172−184.

(16) Delville, M. H.; Barbut, D.; Wattiaux, A.; Bassat, J. M.; Menetrier, M.; Labrugere, C.; Grenier, J. C.; Etourneau, J. Electrochemical fluorination of La_2CuO_4: a mild "chimie douce" route to superconducting oxyfluoride materials. *Inorg. Chem.* **2009**, *48*, 7962−7969.

(17) Chen, J. M.; Nachimuthu, P.; Liu, R. S.; Lees, S. T.; Gibbons, K. E.; Gameson, I.; Jones, M. O.; Edwards, P. P. Hole states in fluorine-doped La_2CuO_4 thin films probed by polarized x-ray-absorption spectroscopy. *Phys. Rev. B: Condens. Matter Mater. Phys.* **1999**, *60*, 6888−6892.

(18) Anisimov, V. I.; Bukhvalov, D.; Rice, T. M. Electronic structure of possible nickelate analogs to the cuprates. *Phys. Rev. B: Condens. Matter Mater. Phys.* **1999**, *59*, 7901−7906.

(19) Poltavets, V. V.; Lokshin, K. A.; Nevidomskyy, A. H.; Croft, M.; Tyson, T. A.; Hadermann, J.; Van Tendeloo, G.; Egami, T.; Kotliar, G.; ApRoberts-Warren, N.; Dioguardi, A. P.; Curro, N. J.; Greenblatt, M. Bulk magnetic order in a two-dimensional Ni^{1+}/Ni^{2+} (d^9/d^8) nickelate, isoelectronic with superconducting cuprates. *Phys. Rev. Lett.* **2010**, *104*, No. 206403.

(20) Poltavets, V. V.; Greenblatt, M.; Fecher, G. H.; Felser, C. Electronic properties, band structure, and fermi surface instabilities of Ni^{1+}/Ni^{2+} nickelate $La_3Ni_2O_6$, isoelectronic with superconducting cuprates. *Phys. Rev. Lett.* **2009**, *102*, No. 046405.

(21) Crespin, M.; Levitz, P.; Gatinea, L. Reduced Forms of $LaNi0_3$ Perovskite Part 1.-Evidence for New Phases: $La_2Ni_20_5$ and $LaNiO_2$. *J. Chem. Soc., Faraday Trans. 2* **1983**, *79*, 1181−1194.

(22) Hayward, M. A.; Green, M. A.; Rosseinsky, M. J.; Sloan, J. Sodium hydride as a powerful reducing agent for topotactic oxide deintercalation: Synthesis and characterization of the nickel(I) oxide $LaNiO_2$. *J. Am. Chem. Soc.* **1999**, *121*, 8843−8854.

(23) Crespin, M.; Isnard, O.; Dubois, F.; Choisnet, J.; Odier, P. $LaNiO_2$: Synthesis and structural characterization. *J. Solid State Chem.* **2005**, *178*, 1326−1334.

(24) Poltavets, V. V.; Lokshin, K. A.; Croft, M.; Mandal, T. K.; Egami, T.; Greenblatt, M. Crystal structures of $Ln_4Ni_3O_8$ (Ln = La, Nd) triple layer T'-type nickelates. *Inorg. Chem.* **2007**, *46*, 10887−10891.

(25) Poltavets, V. V.; Lokshin, K. A.; Dikmen, S.; Croft, M.; Egami, T.; Greenblatt, M. $La_3Ni_2O_6$: a new double T'-type nickelate with infinite $Ni^{1+}/^{2+}O_2$ layers. *J. Am. Chem. Soc.* **2006**, *128*, 9050−9051.
(26) Lacorre, P. Passage from T-Type to T'-Type Arrangement to by Reducing $R_4Ni_3O_{10}$ to $R_4Ni_3O_8$ (R = La, Pr, Nd). *J. Solid State Chem.* **1992**, *97*, 495−500.
(27) Retoux, R.; Rodriguez-Carvajal, J.; Lacorre, P. Neutron diffraction and TEM studies of the crystal structure and defects of $Nd_4Ni_3O_8$. *J. Solid State Chem.* **1998**, *140*, 307−315.
(28) Crespin, M.; Landron, C.; Odier, P.; Bassat, J. M.; Mouron, P.; Choisnet, J. Evidence for nickel-(I)-rich mixed oxide with a defect K_2NiF_4-type structure. *J. Solid State Chem.* **1992**, *100*, 281−291.
(29) Wissel, K.; Heldt, J.; Groszewicz, P. B.; Dasgupta, S.; Breitzke, H.; Donzelli, M.; Waidha, A. I.; Fortes, A. D.; Rohrer, J.; Slater, P. R.; Buntkowsky, G.; Clemens, O. Topochemical Fluorination of La_2NiO_{4+d}: Unprecedented Ordering of Oxide and Fluoride Ions in $La_2NiO_3F_2$. *Inorg. Chem.* **2018**, *57*, 6549−6560.
(30) Wissel, K.; Dasgupta, S.; Benes, A.; Schoch, R.; Bauer, M.; Witte, R.; Fortes, A. D.; Erdem, E.; Rohrer, J.; Clemens, O. Developing intercalation based anode materials for fluoride-ion batteries: topochemical reduction of $Sr_2TiO_3F_2$ via a hydride based defluorination process. *J. Mater. Chem. A* **2018**, *6*, 22013−22026.
(31) Wissel, K.; Vogel, T.; Dasgupta, S.; Fortes, A. D.; Slater, P. R.; Clemens, O. Topochemical Fluorination of n = 2 Ruddlesden-Popper Type $Sr_3Ti_2O_7$ to $Sr_3Ti_2O_5F_4$ and Its Reductive Defluorination. *Inorg. Chem.* **2020**, *59*, 1153−1163.
(32) Asano, H.; Hayakawa, J.; Matsui, M. Giant magnetoresistance of a two-dimensional ferromagnet $La_{2-2x}Ca_{1+2x}Mn_2O_7$. *Appl. Phys. Lett.* **1996**, *68*, 3638−3640.
(33) Wang, A.; Cao, G. Electron-transport and magnetic properties of the layered perovskite $La_{2-2x}Sr_{1+2x}Mn_2O_7$. *J. Magn. Magn. Mater.* **2006**, *305*, 520−523.
(34) Vaknin, D.; Sinha, S. K.; Moncton, D. E.; Johnston, D. C.; Newsam, J. M.; Safinya, C. R.; King, H. E. Antiferromagnetism in La_2CuO_{4-y}. *Phys. Rev. Lett.* **1987**, *58*, 2802−2805.
(35) Takeiri, F.; Yamamoto, T.; Hayashi, N.; Hosokawa, S.; Arai, K.; Kikkawa, J.; Ikeda, K.; Honda, T.; Otomo, T.; Tassel, C.; Kimoto, K.; Kageyama, H. $AgFeOF_2$: A Fluorine-Rich Perovskite Oxyfluoride. *Inorg. Chem.* **2018**, *57*, 6686−6691.
(36) Clemens, O.; Vasala, S.; da Silva, I.; Wissel, K.; Slater, P. *Investigation of $La_2NiO_3F_2$ and Defluorinated Phases with Ruddlesden-Popper Type Structure*; STFC ISIS Neutron and Muon Source, 2018.
(37) Day, P.; Enderby, J.; Williams, W.; Chapon, L.; Hannon, A.; Radaelli, P.; Soper, A. Scientific Reviews: GEM: The General Materials Diffractometer at ISIS-Multibank Capabilities for Studying Crystalline and Disordered Materials. *Neutron News* **2004**, *15*, 19−23.
(38) Hannon, A. C. Results on disordered materials from the GEneral Materials diffractometer, GEM, at ISIS. *Nucl. Instrum. Methods Phys. Res., Sect. A* **2005**, *551*, 88−107.
(39) Arnold, O.; Bilheux, J. C.; Borreguero, J. M.; Buts, A.; Campbell, S. I.; Chapon, L.; Doucet, M.; Draper, N.; Ferraz Leal, R.; Gigg, M. A.; Lynch, V. E.; Markvardsen, A.; Mikkelson, D. J.; Mikkelson, R. L.; Miller, R.; Palmen, K.; Parker, P.; Passos, G.; Perring, T. G.; Peterson, P. F.; Ren, S.; Reuter, M. A.; Savici, A. T.; Taylor, J. W.; Taylor, R. J.; Tolchenov, R.; Zhou, W.; Zikovsky, J. Mantid—Data analysis and visualization package for neutron scattering and μ SR experiments. *Nucl. Instrum. Methods Phys. Res., Sect. A* **2014**, *764*, 156−166.
(40) Diffrac.suite—User Manual TOPAS 5. Bruker AXS: Karlsruhe, Germany, 2014.
(41) Coelho, A. A. TOPAS-Academic. http://www.topas-academic.net (accessed Oct 20, 2014).
(42) Cheary, R. W.; Coelho, A. A.; Cline, J. P. Fundamental Parameters Line Profile Fitting in Laboratory Diffractometers. *J. Res. Natl. Inst. Stand. Technol.* **2004**, *109*, 1−25.
(43) Kolb, U.; Gorelik, T.; Kübel, C.; Otten, M. T.; Hubert, D. Towards automated diffraction tomography: Part I—Data acquisition. *Ultramicroscopy* **2007**, *107*, 507−513.
(44) Plana-Ruiz, S.; Krysiak, Y.; Portillo, J.; Alig, E.; Estradé, S.; Peiró, F.; Kolb, U. Fast-ADT: a fast and automated electron diffraction tomography setup for structure determination and refinement. *Ultramicroscopy* **2020**, No. 112951.
(45) Vincent, R.; Midgley, P. A. Double conical beam-rocking system for measurement of integrated electron diffraction intensities. *Ultramicroscopy* **1994**, *53*, 271−282.
(46) Mugnaioli, E.; Gorelik, T.; Kolb, U. "Ab initio" structure solution from electron diffraction data obtained by a combination of automated diffraction tomography and precession technique. *Ultramicroscopy* **2009**, *109*, 758−765.
(47) Kolb, U.; Mugnaioli, E.; Gorelik, T. E. Automated electron diffraction tomography - a new tool for nano crystal structure analysis. *Cryst. Res. Technol.* **2011**, *46*, 542−554.
(48) Burla, M. C.; Caliandro, R.; Carrozzini, B.; Cascarano, G. L.; Cuocci, C.; Giacovazzo, C.; Mallamo, M.; Mazzone, A.; Polidori, G. Crystal structure determination and refinement via SIR2014. *J. Appl. Crystallogr.* **2015**, *48*, 306−309.
(49) Petříček, V.; Dušek, M.; Palatinus, L. Crystallographic Computing System JANA2006: General features. *Z. Kristallogr. − Cryst. Mater.* **2014**, *229*, 345−352.
(50) Palatinus, L.; Brazda, P.; Jelinek, M.; Hrda, J.; Steciuk, G.; Klementova, M. Specifics of the data processing of precession electron diffraction tomography data and their implementation in the program PETS2.0. *Acta Crystallogr., Sect. B: Struct. Sci., Cryst. Eng. Mater.* **2019**, *75*, 512−522.
(51) Kresse, G.; Hafner, J. Ab initio molecular-dynamics simulation of the liquid-metal–amorphous-semiconductor transition in germanium. *Phys. Rev. B: Condens. Matter Mater. Phys.* **1994**, *49*, 14251−14269.
(52) Kresse, G.; Furthmüller, J. Efficiency of ab-initio total energy calculations for metals and semiconductors using a plane-wave basis set. *Comput. Mater. Sci.* **1996**, *6*, 15−50.
(53) Kresse, G.; Joubert, D. From ultrasoft pseudopotentials to the projector augmented-wave method. *Phys. Rev. B: Condens. Matter Mater. Phys.* **1999**, *59*, 1758−1775.
(54) Blöchl, P. E. Projector augmented-wave method. *Phys. Rev. B: Condens. Matter Mater. Phys.* **1994**, *50*, 17953−17979.
(55) Perdew, J. P.; Burke, K.; Ernzerhof, M. Generalized Gradient Approximation Made Simple. *Phys. Rev. Lett.* **1996**, *77*, 3865−3868.
(56) Dudarev, S. L.; Botton, G. A.; Savrasov, S. Y.; Humphreys, C. J.; Sutton, A. P. Electron-energy-loss spectra and the structural stability of nickel oxide: An LSDA+U study. *Phys. Rev. B: Condens. Matter Mater. Phys.* **1998**, *57*, 1505−1509.
(57) Pardo, V.; Pickett, W. E. Pressure-induced metal-insulator and spin-state transition in low-valence layered nickelates. *Phys. Rev. B: Condens. Matter Mater. Phys.* **2012**, *85*, No. 045111.
(58) Monkhorst, H. J.; Pack, J. D. Special points for Brillouin-zone integrations. *Phys. Rev. B: Condens. Matter Mater. Phys.* **1976**, *13*, 5188−5192.
(59) Dervos, C. T.; Vassiliou, P.; Novacovich, J.; Kollia, C. Vacuum heated electroless nickel plated contacts. *IEEE Trans. Compon. Packag. Technol.* **2004**, *27*, 131−137.
(60) Jović, V. D.; Maksimović, V.; Pavlović, M. G.; Popov, K. I. Morphology, internal structure and growth mechanism of electrodeposited Ni and Co powders. *J. Solid State Electrochem.* **2006**, *10*, 373−379.
(61) Hancock, C. A. Anion Substitution in Perovskite Related Materials for Fuel Cell Applications. Ph.D. Thesis, University of Birmingham: Birmingham, 2012.
(62) Rodriguez-Carvajal, J.; Fernandez-Diaz, M. T.; Martinez, J. L. Neutron diffraction study on structural and magnetic properties of La_2NiO_4. *J. Phys.: Condens. Matter* **1991**, *3*, 3215−3234.
(63) Müller-Buschbaum, H.; Wollschläger, M. W. Über ternäre Oxocuprate. VII. Zur Kristallstruktur von Nd_2CuO_4. *Z. Anorg. Allg. Chem.* **1975**, *414*, 76−80.
(64) Perez-Mato, J. M.; Gallego, S. V.; Tasci, E. S.; Elcoro, L.; de la Flor, G.; Aroyo, M. I. Symmetry-Based Computational Tools for Magnetic Crystallography. *Annu. Rev. Mater. Res.* **2015**, *45*, 217−248.

(65) Patra, L.; Kishore, M. R. A.; Vidya, R.; Sjåstad, A. O.; Fjellvåg, H.; Ravindran, P. Electronic and Magnetic Structures of Hole Doped Trilayer $La_{4-x}Sr_xNi_3O_8$ from First-Principles Calculations. *Inorg. Chem.* **2016**, *55*, 11898−11907.
(66) Freltoft, T.; Buttrey, D. J.; Aeppli, G.; Vaknin, D.; Shirane, G. Magnetic correlations and their dependence on excess oxygen in $La_2NiO_{4+\delta}$. *Phys. Rev. B: Condens. Matter Mater. Phys.* **1991**, *44*, 5046−5056.
(67) Anji Reddy, M.; Fichtner, M. Batteries based on fluoride shuttle. *J. Mater. Chem.* **2011**, *21*, 17059−17062.
(68) Clemens, O.; Rongeat, C.; Reddy, M. A.; Giehr, A.; Fichtner, M.; Hahn, H. Electrochemical fluorination of perovskite type $BaFeO_{2.5}$. *Dalton Trans.* **2014**, *43*, 15771−15778.
(69) Nowroozi, M. A.; de Laune, B.; Clemens, O. Reversible Electrochemical Intercalation and Deintercalation of Fluoride Ions into Host Lattices with Schafarzikite-Type Structure. *ChemistryOpen* **2018**, *7*, 617−623.
(70) Nowroozi, M. A.; Ivlev, S.; Rohrer, J.; Clemens, O. La_2CoO_4: a new intercalation based cathode material for fluoride ion batteries with improved cycling stability. *J. Mater. Chem. A* **2018**, *6*, 4658−4669.
(71) Nowroozi, M. A.; Wissel, K.; Rohrer, J.; Munnangi, A. R.; Clemens, O. $LaSrMnO_4$: Reversible Electrochemical Intercalation of Fluoride Ions in the Context of Fluoride Ion Batteries. *Chem. Mater.* **2017**, *29*, 3441−3453.

https://dx.doi.org/10.1021/acs.chemmater.0c00193
Chem. Mater. 2020, 32, 3160−3179